Assessment of hybrid RANS-LES methods for accurate automotive aerodynamic simulations

P. Ekman [a,*], D. Wieser [b], T. Virdung [c], M. Karlsson [a]

[a] Linköping University, SE58183, Linköping, Sweden
[b] Technische Universität Berlin, DE10623, Berlin-Charlottenburg, Germany
[c] Volvo Car Corporation, SE40531, Göteborg, Sweden

The introduction of the Harmonized Light Vehicles Test Procedure causes a significant challenge for the automotive industry, as it increases the importance of efficient aerodynamics and demands how variations of optional extras affect the car's fuel consumption and emissions. This may lead to a huge number of combinations of optional extras that may need to be aerodynamically analyzed and possibly optimized, being to resource-consuming to be done with wind tunnel testing merely. Reynolds Average Navier-Stoles (RANS) coupled with Large Eddy Simulations (LES) have shown potential for accurate simulation for automotive applications for reasonable computational cost. In this paper, three hybrid RANS-LES models are investigated on the DrivAer notchback and fastback car bodies and compared to wind tunnel measurements. Several yaw angles are investigated to see the model's ability to capture small and large changes of the flow field. It is seen that the models generally are in good agreement with the measurement, but only one model is able to capture the behavior seen in the measurements consistently. This is connected to the complex flow over the rear window, which is important to capture for accurate force predictions.

1. Introduction

Transports are responsible for almost 25 % of the greenhouse gas emission in Europe and are the leading cause of air pollution in cities European Commission (2016a). Of these 25 %, almost half of the carbon dioxide (CO_2) emissions are emitted by passenger cars. Since 2009, the European Commission has introduced legislation for reducing the emissions of new passenger cars. In 2015, a maximum limit of 130 g of CO_2/km was applied as regulation for all new vehicles, as a fleet-wide average. From 2021 the emission target will be lowered even further to 95 CO_2/km. For meeting these emission level criteria, a fuel consumption of around 4.1 $L/100km$ and 3.6 $L/100km$ is needed for petrol and diesel internal combustion engine (ICE) cars, respectively European Commission (2016b).

In 2017, the Worldwide Harmonized Light Vehicles Test Procedure (WLTP) for measuring the emissions and fuel consumption of cars was introduced WLTP Facts (2017). This test procedure has two major effects on the importance of aerodynamics for cars. Firstly, the average speed of the test cycle is increased to 46 km/h, which is 12 km/h higher than in the previously used test cycle (New European Driving Cycle). As aerodynamic forces increase with the square root of the vehicle's velocity

(windless conditions), this makes the aerodynamics more important during the test cycle. For speeds over 80 km/h, the aerodynamic drag is the main energy-consuming source Hucho and Sovran (1993). Secondly, is that the exact configuration of the car that actually is sold to the customer needs to be certified in terms of fuel consumption and emissions. The rationale for this is that customers should be able to have a better understanding of what impact any specific configuration will have on fuel consumption and emissions. This means that any combination of optional extras that the customer can add to the car must be certified with WLTP. For example, the Volvo XC90 can theoretically be *externally* configured in more than 300 000 different combinations Ekman et al. (2019). Of all of these combinations, more than 200 specific combinations may, in fact, have a significant impact on the aerodynamics and therefore need to be analyzed and possibly optimized. For electric vehicles, this has no impact on the emissions but instead directly affects the range of the vehicle. The energy losses from aerodynamic drag is reported to be 4.4 times larger for electric vehicles (EV) than seen for ICE vehicles Kawamata et al. (2016), resulting in even more importance for efficient aerodynamics. In 2019 Audi AG stated that 5 drag counts (one drag count = $\Delta C_D \cdot 10^{-3}$) corresponded to a 2.5 km in range of their fully electric SUV Audi AG (2019). This may result in that optional extras, such

---

as rims, spoilers, towbar and roof-rails, directly affect the range of the vehicle.

Traditionally wind tunnel testing has been the main tool for the aerodynamic development of vehicles, but with the introduction of WLTP, which drastically increases the number of necessary aerodynamic design analysis, and the ever more importance for efficient aerodynamics of electric vehicles, Computational Fluid Dynamics (CFD) cannot merely be a complement to wind tunnel testing during development. Today accurate CFD methods exist, as the Scale-Resolving Simulation (SRS) method Large Eddy Simulations (LES) have shown excellent agreement to measurements for flow around bluff bodies Krajnović and Davidson (2004), Hinterberger et al. (2004), Serre et al. (2013). Unfortunately, LES is, for most cases not feasible, due to the very high computational cost, especially for the moderate to high Reynolds numbers that typically are used during aerodynamic development of cars. Historically, Reynolds Average Navier-Stokes (RANS) simulations have been performed as a complement to wind tunnel testing during the aerodynamic development. In RANS, the behavior of all the turbulence is modeled, which makes it possible to use a significantly coarser spatial resolution than for LES, resulting in lower computational costs. However, the flow around bluff bodies and vehicles are highly time-dependent and unsteady, typically causing RANS methods to struggle to capture details of the flow accurately. Reasonable accurate drag predictions are possible with RANS but can be very case dependent Guilmineau (2014), Ashton and Revell (2015), Ashton et al. (2016), Rodi (1997), making it unreliable for accurate aerodynamic development. For solving the high-cost deficits of LES and lower accuracy of RANS, hybrid RANS-LES methods have become popular. The most common method is the Detached Eddy Simulation (DES) approach, where RANS is used to model the near-wall flow while LES is employed elsewhere in the domain Spalart (1997). As RANS is used near the wall, a coarse spatial resolution (compared to LES) is possible in the near-wall region, while a finer spatial resolution (compared to RANS) only is needed where turbulence is resolved. This approach greatly reduces the overall mesh size and also the required temporal resolution compared to LES.

The original DES model proposed by Spalart et al. Spalart (1997) is accurate for flow with thin boundary layers and massive separations (which was the designated intention of the model) but struggle in flows with thick boundary layers and shallow separations Spalart et al. (2006). This is due to the mesh size parallel to the wall being smaller than the thickness of the boundary layer, causing the DES model to switch to LES too early, which often lead to under-resolved Reynolds stresses and thereby too low skin friction, resulting in premature separation known as Grid Induced Separation (GIS) Spalart et al. (2006).

In 2006 an improvement of the DES model was published by Spalart et al. Spalart et al. (2006), called Delayed DES (DDES), which utilizes a stronger shielding of the RANS region in order to be significantly less sensitive to GIS. In 2008 Shur et al. Shur et al. (2008) released an improved version of the DDES model, Improved DDES (IDDES), which includes wall model possibilities for LES in order to broaden the application areas for the model. IDDES is designed to behave as DDES but with the possibility to switch from RANS to Wall Modeled LES (WMLES) for the near-wall flow if enough unsteadiness occurs Shur et al. (2008). Due to this, DDES and IDDES have become popular models for aerodynamic predictions within the automotive community Guilmineau (2014), Ashton and Revell (2015), Ashton et al. (2016), Sterken et al. (2016), Ashton et al. (2018), Tunay et al. (2020) and showed good agreement with measurements.

Two major challenges with DES methods is the ability to shield the RANS region during mesh refinement and ensure a fast transition between the RANS and LES regions. The first is vital to reducing possibilities to GIS and user dependency, as less awareness of the RANS to LES switching effects of the mesh is needed. Fast transition between RANS and LES reduces the so-called gray-area, which is a region where the initial lack of resolved turbulence results in a sort of pseudo-laminar-turbulent transition occurs before fully developed resolved turbulence

is achieved further downstream Mockett (2009). Fast transition between the regions is, therefore, especially important for accurate predictions of separating shear layers Menter (2016), being an essential flow feature of car aerodynamics.

In recent time several models have been proposed which attempts to solve these major challenges, such as the $\varphi - f$ elliptic relaxation model Ashton et al. (2011), Stress Blended Eddy Simulation (SBES) Menter (2016) and the σ-DDES approach Nicoud et al. (2011), Fuchs et al. (2020).

Historically most validation and sensitivity studies for CFD within the automotive sector have been performed on simplified generic car bodies, such as the Ahmed body Ahmed et al. (1984) and the SAE body Le Good and Garry (2004). However, such simplified car bodies do often only resemble some of the aerodynamic features of ground vehicles. To fill the gap between the too generic bluff bodies and fully detailed production cars that are not public, TU Munich, in cooperation with car manufacturers Audi AG and BMW, designed and released the generic DrivAer car body Heft et al. (2012). The DrivAer design is a hybrid of the Audi A4^{TM} and BMW 3-series^{TM} and exists as a mid-size car and SUV Zhang et al. (2019) in three different rear end configurations, fastback, notchback, and estate, respectively. The aerodynamic resemblance of a production car has made it a popular validation and reference case for both wind tunnel measurements and CFD simulations.

Although the DDES and IDDES models have shown good correlation to wind tunnel measurements for the DrivAer car body (Ashton and Revell (2015); Ashton et al. (2016); Collin et al. (2016); Wang et al. (2019)) there is still room for improvement, especially for the flow over the rear part of the body. The fastback and notchback rear end configurations of the DrivAer car body have in wind tunnel measurements shown complex flow over the rear window with shallow separations affected by A and C-pillar vortices Wieser et al. (2014, 2015a). This type of flow is very challenging for hybrid RANS-LES models and includes features where models with improved RANS-LES region transitioning have shown significant improvements over the DDES model Fuchs et al. (2020). Accurate prediction of these complex and sometimes small details of the flow field can be crucial for accurately predicting changes to the forces with changes in the flow conditions.

In this paper the DDES and IDDES models are compared to the recently released SBES model for the flow around the notchback and fastback DrivAer car bodies, to see if stronger RANS shielding and faster transition between the RANS and LES regions improves the aerodynamic accuracy simulation of cars, and therefore is to be recommended for use during aerodynamic development. Specific focus is on the complex flow over the rear window and wake of the car bodies, as these region includes separating shear layers and is responsible for a significant part of the drag.

The DrivAer notchback and fastback configurations with the closed engine bay and flat underbody are chosen for this study, as extensive wind tunnel measurement data exist for these configurations Heft et al. (2012), Strangfeld et al. (2013), Wieser et al. (2014, 2015a, 2015b). Although the flat underbody may not accurately resemble ICE cars, it is well aligned with what is seen for electric cars Palin et al. (2012), Audi AG (2019). On the road, vehicles are rarely subjected to only 0° yaw conditions. Even small degrees of yaw angles can cause significant changes to the flow field and the aerodynamic forces Hucho and Sovran (1993), Bello-Millan et al. (2016), Cheng et al. (2019) and therefore is an important feature that CFD simulations need to be able to capture. In D'Hooge et al. (2014), Kawamata et al. (2016), it is seen that the highest probability of yaw angle in the US is between 1 and 5°, with a fast decrease to around 7° yaw. The notchback configuration has in earlier studies Wieser et al. (2014, 2015a) show to have an asymmetric complex flow behavior over the rear window (even at 0° yaw), making it a very tough test case for hybrid RANS-LES models. Hence the notchback model is subjected to a detailed yaw sweep analysis consisting of five yaw angles between 0° and 7°. A less complex flow has been observed for the fastback configuration Wieser et al. (2014) and is therefore analyzed only for two yaw angles, 0° and 5°.

2. Method

In this section, the set-up of the DrivAer model for the simulations and measurements are presented, followed by descriptions of the used mesh, boundary conditions, numerics, and experimental measurements. Lastly, the variables for post-processing are presented.

2.1. Problem set-up

To ensure similar flow conditions as in the experiments and a fair comparison to the measurement Strangfeld et al. (2013), Wieser et al. (2014, 2015b, 2015a), a large section of the GroWiKa tunnel is included in the simulation domain, Fig. 1. The domain includes the 6.25:1 contraction upstream to the test-section, the test-section and its components and a straight tunnel section downstream of the test section. The DrivAer body used in the wind tunnel measurements and CFD simulations is 1:4 scale, with the length, L, of 1153 mm, and has no engine bay and a smooth underbody. The cross-sectional area of the test-section is $2000 \times \sqrt{2000}$ mm, which results in a solid blockage of 5.4 % at 0° yaw. No moving belt was available in the measurements, resulting in stationary wheels with a flat contact path for both the measurements and simulations. The car body is suspended 2 mm above a splitter plate by a circular balance at the center of the body. The DrivAer body is rotated with the balance to simulate yaw conditions. The balance is covered by a NACA0025 stilt but leaves a small gap of 3.3 mm to DrivAer body underside. The NACA0025 stilt is always set to 0° in the measurements and hence in the simulations. The splitter plate starts $0.58L$ upstream of the car body and extends $0.58L$ downstream it. In the simulation model, some minor simplifications are done to the wind tunnel domain and the DrivAer model for ease of meshing. This includes removal of the pressure probe holes in the DrivAer body and the small gap (< 2 mm) between the splitter plate and the turntable. More information about the experimental set-up can be found in Strangfeld et al. (2013), Wieser et al. (2014, 2015a, 2015b).

2.2. Numerical grid

The numerical grid consists of a triangle surface mesh connected to a Cartesian grid using tetrahedral and pyramid cells. A grid sensitivity study of the notchback configuration at 5° yaw shows that only small differences of the forces exist between the grids consisting of 102 and 158 million cells, Table 1. More significant differences of the forces are seen to a coarser grid consisting of 61 million cells. The grid sensitivity was performed with the SBES model, which ensures sufficient shielding of the RANS region even under severe grid refinements Menter (2016), to ensure a sufficiently fine grid for both the RANS and LES regions. A fine temporal resolution was used for the grid sensitivity investigation, corresponding to a normalized time step $((\Delta t \cdot U_\infty)/L)$ of $4.80 \cdot 10^{-5}$, see

Table 1
Drag and lift coefficients for the three different mesh sizes. Only small differences of the forces are seen between the meshes consisting of 102 and 158 million cells.

Number of cells	C_D	C_L
$61 \cdot 10^6$	0.266	−0.120
$102 \cdot 10^6$	0.268	−0.136
$158 \cdot 10^6$	0.269	−0.137

Ekman et al. (2019), ensuring that >99.99 % of the cells in the whole domain had a Courant-Friedrichs-Lewy (CFL) value below unity. From the grid sensitivity, the grid consisting of 102 million cells (medium mesh in Ekman et al. (2019)) is deemed fine enough to capture the essential flow features and details.

The surface mesh on the car body varies between 0.5 and 2.82 mm and reaches a maximum of 100 mm on the tunnel walls furthest away from the test-section. Between 17 and 20 prisms layers are used on the car body, while 15 layers are used on the wind tunnel wall and components. The first cell height is kept between 0.01 and 0.18 mm on the car body to ensure a $y^+ \leq 2$, Fig. 1. Up 1.2 mm first cell height is used on the tunnel walls downstream of the test-section and ensures a maximum $y^+ \leq 5$ in the domain. The growth rate of the prisms layers, as well as transition to other cells in the domain, are kept below 1.2, Fig. 2. In order to capture the gradients, volume grid refinements are done near the car body, in the wake, and within the test-section, Fig. 2. The cell size in the volume refinement surrounding the vehicle and wake is no larger than 3.55 mm. The volume refinements also account for the enlarged wake during the yaw simulations. Skewness (equilateral volume deviation skewness) of the surface and volume grid was kept below 0.5 and 0.9, respectively. For more information about the grid and the grid sensitivity analysis, see Ekman et al. (2019).

2.3. Numerical set-up

The inflow in the domain is modeled with a uniform velocity profile together with a low turbulence intensity of 0.1 % and turbulent viscosity ratio of 200, to replicate the effects of the honeycomb and turbulent reduction screen located in the large tunnel section of the physical tunnel. The inflow velocity is set to 6.075 m/s and results in a freestream velocity of 39.5 m/s at the location of the pitot tube in the test-section and a Reynolds number of $3.12 \cdot 10^6$, based on the length of the DrivAer body. The walls in the large tunnel section are modeled with free-slip due to the presence of the honeycomb and turbulent reduction screens located in the measurements, Fig. 1. The turbulence properties at the inlet are verified to result in less than 0.5 % turbulence intensity at the test-section, as seen in Wieser et al. (2014). The inlet of the domain is located $6L$ from the start of the test-section. The outflow of the domain is modeled with a zero gauge pressure-outlet and positioned $8.67L$ from the
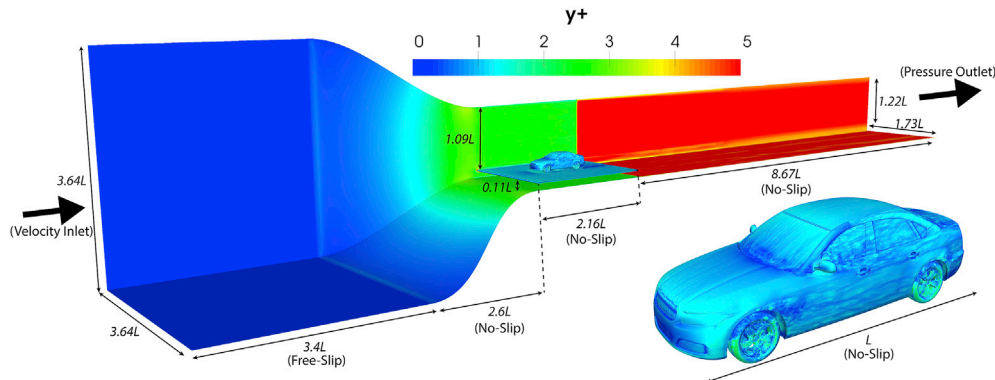

Fig. 1. Geometrical representation of the domain and boundary conditions used for the simulations colored here with the dimensionless wall distance (y^+). Values of around 1 are seen on the car body, while slightly higher values (≤ 5) occur in the test-section and downstream of it.
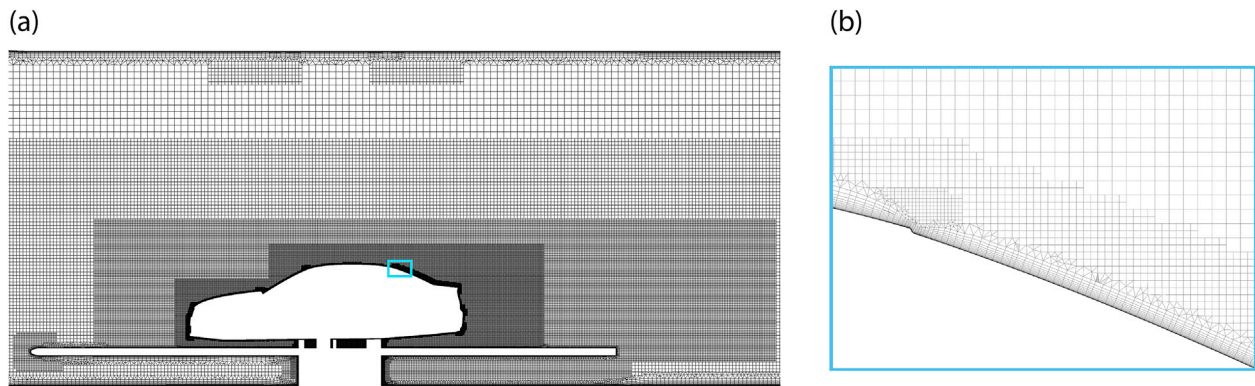
(a)

(b)

Fig. 2. (a) Overview of the grid and its refinements in the domain symmetry plane (y = 0). (b) zoom of the near-wall mesh at the rear window of the notchback configuration.

end of the splitter plate. The walls of the contraction, test-section, and the DrivAer body are modeled as no-slip walls. The set-up follows the best-practice for external aerodynamic simulations SAE Standard J2966 (2013), Lanfrit (2005).

The numerical method used here follows the numerical set up used in Ekman et al. (2019) and is therefore only shortly presented here. The cell-centered finite volume solver ANSYS Fluent 19.0 is used for all simulations. The pressure-based solver is used together with the Semi-Implicit Method for Pressure Linked Equations-Consistent (SIM-PLEC) pressure-velocity coupling scheme. The spatial discretization of the convective terms in the momentum equation is calculated by use of the bounded central differencing scheme, which enables low numerical diffusion by use of the central differencing scheme, but still ensures stability by blending in first and second-order upwind schemes when the convection boundedness criterion is violated Leonard (1991), Jasak et al. (1999). Spatial discretization for the gradients is solved by using the least-squares cell-based method, while the pressure is solved with the central difference scheme. The first-order upwind scheme is used for the RANS turbulence equations (k and ω) used in the RANS region. Sensitivity tests have been performed with the second-order upwind scheme for the RANS turbulence equations (k and ω) but resulted in very small changes in the flow field and drag force ($\Delta C_D \leq 0.002$) for the notchback configuration.

For the transient formulation, the second-order bounded implicit iterative time-advancement is used. Six inner loop iterations for every time step is used to ensure a convergence of all normalized residuals below 10^{-5} for the instantaneous solution. In Ekman et al. (2019), the sensitivity of changing the time-step size was investigated for the notchback body at 5° yaw with the SBES model. It was seen that using a normalized time-step size (($\Delta t \cdot U_\infty$)/L) of $9.59 \cdot 10^{-4}$, only caused minor differences to the flow field and the forces, when compared to a normalized time step of $4.80 \cdot 10^{-5}$ being the reference. This resulted in less than 1.1 drag counts, and 8 lift counts difference while reducing the simulation time with 90.2 %. With this time-step size, 88 % of all the cells in the LES region are within the CFL ≤ 1 criterion. With the accuracy kept at a reasonable level and the significantly reduce simulation time, the normalized time-step size of $9.59 \cdot 10^{-4}$ is used throughout this study. All simulations are initialized from a steady-state RANS simulation performed with the $k - \omega$ SST model Menter (1994), where the velocity field has been turned unsteady using vortex synthesizer. The simulation then runs for 20 convective flow units (t = $20L/U_\infty$) to ensure an established continuing state. Another 20 convective flow units are simulated for time-averaging, resulting in less than a half drag count fluctuations of the moving mean value.

Three hybrid RANS-LES models are investigated in this study: DDES, IDDES, and SBES. The models are based on or similar to the original DES model proposed by Spalart et al. Spalart (1997) by using RANS modeling of the near-wall region and LES to resolve turbulent structures further

away from the wall. Both the IDDES and SBES models have the ability to switch from RANS to WMLES for the near-wall flow, when enough unsteadiness upstream exists, thereby resolving some of the turbulent structures in the near-wall region. In this study, the $k - \omega$ SST RANS model is used as the RANS model for the investigated hybrid RANS-LES models, to ensure a fair and straightforward comparison between the hybrid RANS-LES methods.

A significant difference for the SBES model compared to DDES and IDDES models is that it uses a shielding function to switch between a RANS and LES model. In this study, the dynamic Smagorinsky-Lilly Sub-Grid Scale (SGS) model Germano et al. (1991) is used within the LES region for the SBES model. The shielding function has the ability to shield the RANS region during severe mesh refinements Menter (2016). Due to the much stronger shielding, a tweaked definition of the LES length scale can be used, enabling a significant faster transition from the RANS to LES region and lower turbulent viscosity levels within the LES region Menter (2016). This results in more resolved turbulence within the beginning of the LES region, making it especially suitable for separation shear layers. A similar definition can also be implemented for the DDES and IDDES models but would results in much worse RANS shielding.

One simulation is also performed with the IDDES model using the Spalart-Allmaras RANS model (here called IDDES SA) Spalart and Allmaras (1992) to see the RANS model's effects on the WMLES switching in the IDDES model. The implementation of the DDES and IDDES models with the $k - \omega$ SST RANS model used in this study are based on investigations in Gritskevich et al. (2012), Gritskevich et al. (2013). For more information about the hybrid RANS-LES models in this study, see Spalart (1997), Spalart et al. (2006), Shur et al. (2008), Menter (2016).

2.4. Experimental measurements

The experimental measurements were performed for a Reynolds number of $3.2 \cdot 10^6$, based on the length of the DrivAer model Wieser et al. (2014, 2015a). All aerodynamic forces were measured with an external 6-component balance located beneath the measurement section. The maximum measurement error is 0.1 % full scale at a maximum measurement range of 2200 N. The measured forces are averaged over 128 s with a sampling rate of f = 5Hz. The surface pressure distribution at the rear of the model and in the plane of symmetry are captured by 211 and 143 pressure taps for the fastback and notchback configurations, respectively. Most of the pressure taps are located on one side of the model to increase the spatial resolution of the measurements. A higher density of the pressure taps is used where high surface pressure gradients are expected, e.g., at the C-pillars. The pressure measurements are performed for both the positive and negative yaw angled in order to get the pressure distribution for both sides of the model. Some reference taps exist on the opposite side to ensure consistent measurements. In the present study, 74 synchronized and time-resolved piezo-resistive

differential pressure sensors are available for pressure fluctuation measurements. The sensors are located within the model, giving a distance between 40 and 50 mm between the sensor membranes and the surface of the model. The pressure range of the sensors is ±1000 Pa at a resolution of 16 bits and a maximum sensor error of 0.5 % full scale. All pressure measurements are performed with a sampling rate of 4096 Hz and a during 128 s. To collect data from all pressure taps, several tests are conducted and subsequently merged to produce an overall result. The reference static pressure for the differential pressure sensors is taken from a pitot tube located at the wind tunnel ceiling. The flow field of the wake in the plane of symmetry is exposed utilizing Stereo Particle Image Velocimetry (PIV) by a laser light plane with 2 mm thickness and DEHS droplets of 1 μm in nominal diameter. The PIV system's time resolution is $f = 5 Hz$, with a pulse distance between two double images of 20 µs. The recorded images have a resolution of 2048 × 2048 pixels, and two xz-planes with an overlap of 150 mm are measured to capture the entire wake. For each measurement, 1100 pairs of images are recorded, to ensure convergence of the mean values. For more information about the measurement see Wieser et al. (2014, 2015b, 2015a).

2.5. Post-processing

Only normalized time-averaged quantities, except for the Q-criterion, are presented in this study (both measurements and simulations). Normalized forces are calculated according to Equation 1

$$C_{(D,L)} = \frac{F_{(D,L)}}{\left(0.5\rho_\infty((1+\varphi)U_\infty)^2 A\right)} \tag{1}$$

where F_D is the drag force, F_L the lift force, ρ_∞ is the density of the air, φ the percentage solid blockage of the DrivAer model in the test-section, U_∞ the air velocity and A the projected frontal area of the car model. Blockage correction is applied to reduce the effect of the tunnel on the measured and calculated forces. A equals 0.135 m^2 for 0° yaw and is kept constant during the investigation. The density, velocity, and reference static pressure, p_∞, are measured at a pitot tube located in the sealing of the test-section, 240 mm downstream of the contraction. The surface pressure coefficient is calculated with Equation (2) and includes subtraction of the reference pressure in the test-section.

$$C_P = \frac{p - p_\infty}{\left(0.5\rho_\infty U_\infty^2\right)} \tag{2}$$

The normalized fluctuating pressure coefficient, $C_{P,RMS}$, is calculated with Equation (3):

$$C_{P,RMS} = \frac{p'}{\left(0.5\rho_\infty U_\infty^2\right)} \tag{3}$$

Here p' is the fluctuating pressure during the simulation and is achieved from $p' = p - \overline{p}$, where $\overline{p}$ is the time-averaged pressure. The pressure distribution from the measurement is interpolated between the pressure taps. As dense pressure measurements are only performed for one side of the car model, it consists of two pressure maps merged together; hence full continuity at the symmetry line of the car might not always be achieved. For 0° yaw, the pressure distribution is mirrored around the car symmetry line, forcing it to be symmetrical. The skin friction coefficient is calculated using Equation (4), where τ is the computed wall shear stress.

$$C_f = \frac{\tau}{\left(0.5\rho_\infty U_\infty^2\right)} \tag{4}$$

Focus points, saddle points, as well as stable and unstable nodes, are found where the skin friction approach zero ($C_f \to 0$). The bifurcation lines are found where the dividing skin friction line exists. For the simulations, the resolved part of the turbulent kinetic energy (TKE), k_{res}, is monitored and compared between the investigated models, Equation (5).

$$\frac{k_{res}}{U_\infty^2} = \frac{0.5(\overline{u'^2} + \overline{v'^2} + \overline{w'^2})}{U_\infty^2} \tag{5}$$

In Equation (5), u', v' and w' are the fluctuating velocity components in the x, y and z directions, respectively.

3. Results and discussion

The results section starts with the effect of the drag and lift forces when changing the yaw angle. This is followed by comparison, between measurement and simulations, of the rear wake of the notchback vehicle, which accounts for a significant part of the drag for vehicles. The near-wall flow field is then investigated to see how well the hybrid RANS-LES models predict the flow field over the rear end of the car configurations, a region including shallow separations Wieser et al. (2014, 2015a), Ekman et al. (2019). The surface pressure measurement of the rear part of the car configurations is then compared to the simulations. As the flow over, especially the rear part of, the vehicle is unsteady, a comparison of pressure fluctuations is presented to see how well the hybrid RANS-LES models predict the unsteady flow. Lastly, the modeling behavior between the hybrid RANS-LES models is presented.

3.1. Aerodynamic forces

To investigated the highest likely yaw angles occurring in the US D'Hooge et al. (2014), Kawamata et al. (2016), the forces of the notchback and fastback configurations are analyzed between 0° and 7° yaw, Fig. 3. Five yaw angles are simulated for the notchback, as it is expected to be the most challenging case of the car bodies, due to its complex flow behavior over the rear window, while the fastback is simulated for two yaw angles, 0° and 5°. From the measurement, it can be seen that the drag force for the notchback configuration increases linearly with the yaw angle, Fig. 3 panel a. The SBES model is consistent with this and is within the tolerance range of the measurement throughout the yaw sweep. The DDES and IDDES models are not consistent with the measured drag of the notchback configuration, as they only are within the measured tolerance range for a few yaw angles.

It should be noted, that the differences for the DDES and IDDES models to the measurements are rather small throughout the yaw sweep, as often less than five drag counts differ to the error margin of the measurements of ±2.2 drag counts. A drag coefficient of 0.258 was reported by Heft et al. (2012) for the same DrivAer configuration with stationary ground and wheels at 0° yaw, well-aligned to what is seen in this study, with only a few drag counts (≤ 3) difference from the measurement. Note that also the IDDES SA model is included for this configuration, to see how the RANS model affect the switching to the WMLES mode (later discussed in the paper).

Less increase of drag is seen when increasing the yaw angle for the fastback configuration, Fig. 3 panel c. More attached and stable flow over the rear end of the fastback configuration Wieser et al. (2014), compared to the notchback, is the believed reason for this. Opposite to the measurement by Heft et al., 2012, higher drag is seen for the fastback configuration at 0° yaw in the measurements. For this configuration, all the hybrid RANS-LES models underpredict the drag at 0° yaw. The DDES model is in the best agreement with the measurement, with the SBES model not far off. The drag values obtained with the DDES and SBES models are similar to the measured value in Heft et al. (2012) of $C_D = 0.254$, for the same car configuration with stationary ground and wheels at 0° yaw. When increasing the yaw angle to 5°, the DDES model correlates well to the measured drag, while both the IDDES and SBES models still are underpredicting the drag.

The highest lift force values are seen at 0° yaw for both the notchback and fastback configurations in the measurements, Fig. 2 panel b and d. Negative lift force is measured for both car configurations over the yaw sweeps, mainly caused by the smooth underbody with a raised section at the rear acting as a diffuser. In the measurements, the lift force decrease
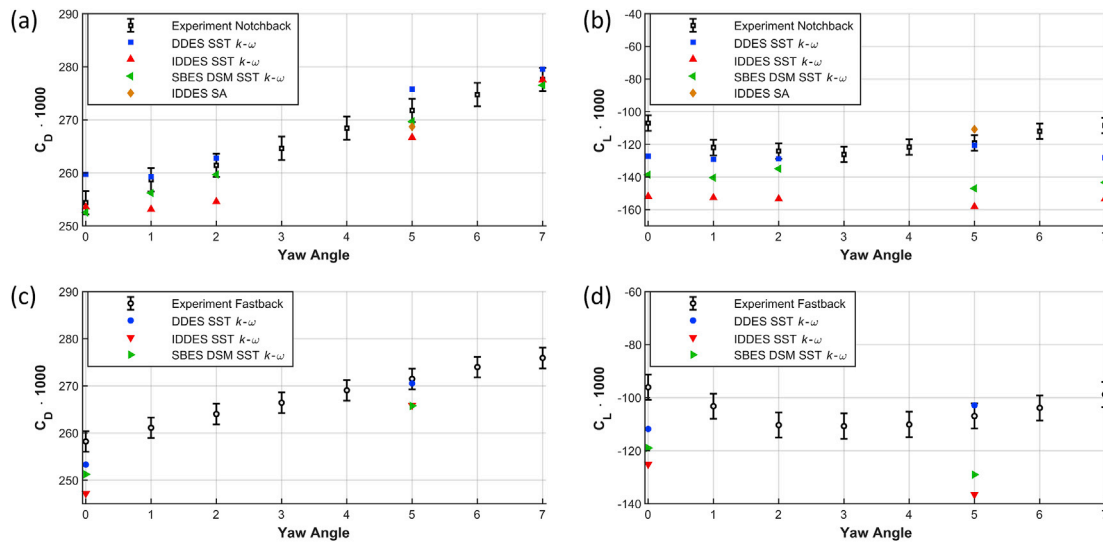
Fig. 3. Drag and lift force coefficients for the investigated yaw sweep for both the wind tunnel measurements and the hybrid RANS-LES models. In (a) and (b), the drag and lift forces are seen for the notchback car configuration, while the drag and lift forces for the fastback configuration are seen in (c) and (d), respectively.

when increasing the yaw sweep up until 3°, where both car configurations achieve its lowest values. The lift force then increases back to the level seen for 0° with increasing yaw. Overall, the DDES model is closest to the measured lift values for both car configurations, while the IDDES and SBES models underpredict the values throughout the yaw sweep. There may be several factors that are influencing the differences between the simulations and measurements. In the measurements, 0° yaw is obtained by changing the angle of the car model until the side force is zero. It can, however, be seen that even small yaw angles changes cause significant changes to the lift force, indicating high sensitivity in the set-up Cheng et al. (2019). It is also not surprising that the most significant differences are seen for the lift force between the measurements and simulations. Small pitch and roll changes can cause significant changes in the absolute measured values, and to ensure that the exact theoretical position of the model is obtained during measurements is difficult.

In aerodynamic development, the importance of accurately estimating the absolute forces is high. However, it is even more critical to accurately predict the changes caused by different flow conditions or

geometrical changes, as is the case for the WLTP legislation. In Fig. 4, the change of the drag and lift forces are seen when increasing the yaw angle for each configuration. The differences are compared against the 0° yaw, as it is the most common yaw angle for the aerodynamic development of passenger cars.

A linear increase of drag is observed in the measurements when increasing the yaw angle for the notchback configurations, Fig. 4 panel a). For the investigated yaw range, a maximum of 23 drag counts increase occurs at 7° yaw for the measurement. At 5° yaw, 17.4 drag counts increase occurs, equaling an increase of 6.8%, being close to the median of drag increase seen for seven production cars in Windsor (2014). The investigated hybrid RANS-LES models are able to capture the general increase of drag over the yaw sweep. However, the SBES model is almost identical to the measurements, with a maximum of a single drag count difference occurring at 1° and 7° yaw. Both the DDES and IDDES models are relatively close to the measurement for the two higher yaw angles (5° and 7°) while struggling at the lower yaw angles. At 1° of yaw, the DDES and IDDES model predicts the wrong trend, as a small decrease of drag is
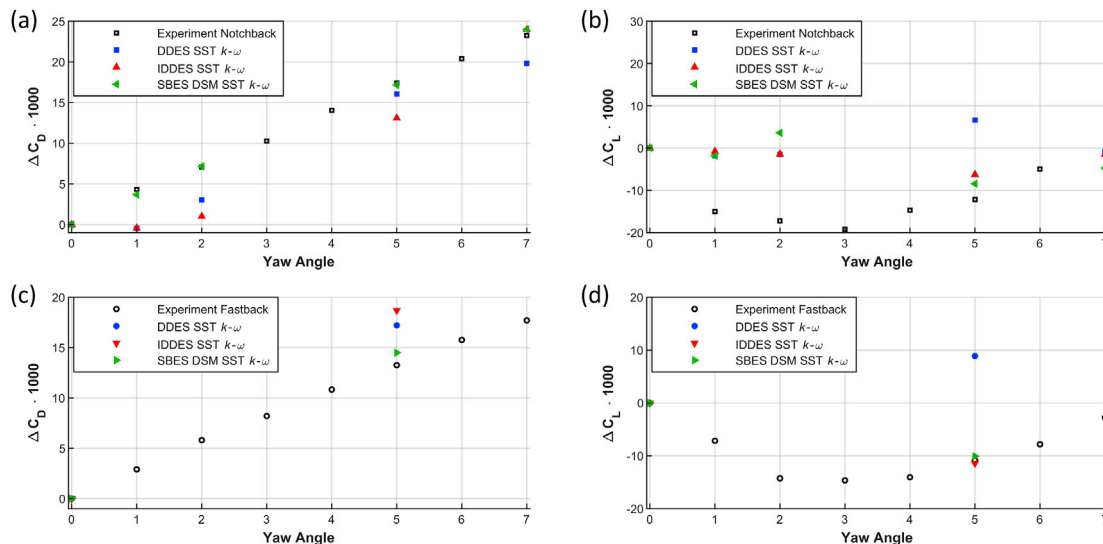

Fig. 4. Drag and lift force coefficients differences for changing the yaw angle from 0° yaw for the measurements and the hybrid RANS-LES models. In (a) and (b), the drag and lift forces differences are seen for the notchback car configuration, while the drag and lift forces differences for the fastback are seen in (c) and (d), respectively.

6

predicted. Less increase of drag with the yaw angle is seen for the fastback configuration, Fig. 4 panel c. At 5° yaw, 13.2 drag counts increase is observed, equaling a drag increase of 5.1%, corresponding to the lower range in Windsor (2014). Here, as for the notchback, the SBES model is closest to capture the drag increase and is within two counts accuracy. Opposite to the notchback configuration, both the DDES and IDDES models overpredict the drag change for the fastback, with more than four drag counts.

For the change of the lift force difference over the yaw sweep, a more closely matched behavior of the hybrid RANS-LES models are seen, Fig. 4 panel b and d. For the notchback configuration, none of the models can capture the measured 15, and 17 counts lift force decreases when increasing the yaw angle to 1° and 2°, respectively. More accurate predictions are seen first at 5°, where both the IDDES and SBES models capture the measured lift force change caused by the yaw change for both car configurations. Here, the DDES model predicts the wrong trend direction. For the notchback configuration at 7° yaw, all the models are close to the measured lift change.

When changing from the notchback to fastback configuration, a drag increase is seen in the measurement at 0° yaw, Fig. 5 panel a. This is opposite to the findings in Heft et al. (2012), where a drag reduction of 4 drag counts is observed at 0° yaw for the same configuration change. None of the hybrid RANS-LES models can capture the measured configuration difference at 0° accurately but are more similar to Heft et al. (2012). The main reason for the wrong trend direction originates from the fact that all the hybrid RANS-LES models are under predicting the absolute drag value for the fastback configuration. For 5° yaw angles, a small drag reduction is observed in the measurement, in which the hybrid RANS-LES models better resemble. Here, the IDDES model is within a single drag count difference to the measured difference. However, the SBES model is the only model to capture the correct drag trend direction when increasing the yaw angle from 0° to 5°, Fig. 5 panel c.

For the lift force change (Fig. 5 panel b), an increase in lift occurs when changing from the notchback to the fastback configuration. Here, both the DDES and SBES models are in reasonable agreement with the measurements, while the IDDES model overpredicts the change significantly. The DDES model is the only model to predict the correct trend prediction of the lift change when increasing the yaw angle to 5°, Fig. 5 panel c.

3.2. Rear wake

More than 15% of the drag occurs at the base of the notchback at 0° yaw. Capturing the rear wake is, therefore, crucial for accurate drag predictions. In Fig. 6, the x-velocity equal to zero isoline is seen for the measurement and simulations for the notchback configuration at 0° yaw. The hybrid RANS-LES models are close to the PIV measurement, especially for the bottom side of the wake. The DDES model underpredicts the

length of the wake, while the overall shape is captured accurately. The IDDES model captures the length of the wake well, but with a slight shift upward. The SBES model agrees best with the PIV measurement, as both the wake endpoint and the free stagnation point are within 0.005L of the measurement, Fig. 6 b). The free stagnation point equals where both the x (u) and z-velocity (w) are zero. The DDES and IDDES models are more than twice the distance from capturing these points, and the DDES model fails to capture the upward position of the free stagnation point relative to the wake endpoint. All the RANS-LES models capture the zero x-velocity behavior close to the base.

3.3. Near-wall flow

The flow over the rear of the DrivAer notchback configuration has in earlier studies Wieser et al. (2014, 2015a), Ekman et al. (2019) seen to have a complex asymmetric flow behavior over the rear window, even at 0° yaw. This is not a specific DrivAer phenomenon, as similar behavior has earlier been observed for notchback car configurations Gaylard et al. (2007), Sims-Williams et al. (2011), Lawson et al. (2007). In Figs. 7 and 8, oil film visualization from the experiments and time-averaged skin friction lines from the simulation are compared for the rear part of the notchback and fastback configurations, respectively, at 0° and 5° yaw. The spanwise skin friction is added in the simulation visualization for easier identifying of the near-wall flow behavior. For identifying of the most dominating skin friction structures, notations (based on the rules of critical point theory) for focus points (notated with F and circles), unstable nodes (notated U), saddle points (notated S) and bifurcation lines (notated B) are added to the figures.

In Fig. 7 panel a, it is seen for the measurement that the flow over the central section of the notchback configuration at 0° yaw is dominated by a large asymmetrical separation bubble, seen by the large region of the white oil film. Almost identical behavior of the near-wall flow structures is seen in Gaylard et al. (2007) for a production notchback car body. The SBES model agrees well with the asymmetric oil film visualization, as it captures the asymmetric separation bubble behavior over the rear window. It is seen that the near-wall flow of the central section of the rear window is dominated by three stable focis (circles) for the SBES model, Fig. 7 panel a. These three stable focis are seen to also exist in the experimental visualization, for the dense region of the oil film and the rotational behavior of the oil film streaks just outside it. The SBES model near-wall field also shows an unstable node (U_R) and a saddle point (S_R). The saddle point (S_R) is located just northeast of the most east stable focus point, while the unstable node (U_R) is northwest of the most west stable focus point. This pattern corresponds well to the interpretation of the near-wall field seen in Gaylard et al. (2007). Indications of the unstable node U_R exist in the experimental visualization, as less dense oil film is seen for the top right side of the separation bubble.
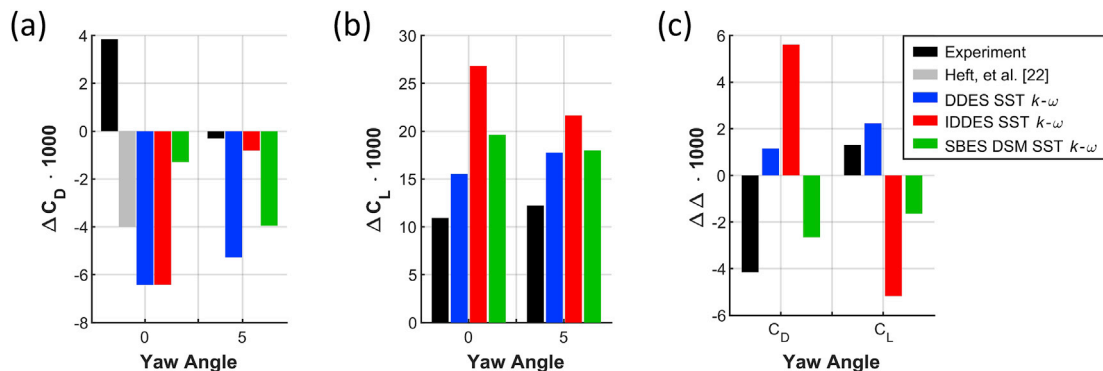

Fig. 5. Drag (a) and lift (b) force coefficients changes when changing from the notchback to fastback configuration for 0° and 5° yaw, for measurements and simulations. In (c), the changes of drag and lift between 0 and 0° and 5° yaw is seen for the configuration changes for the measurement and simulations. Note that measurements from Heft et al. [22] only exist for drag at 0° yaw.
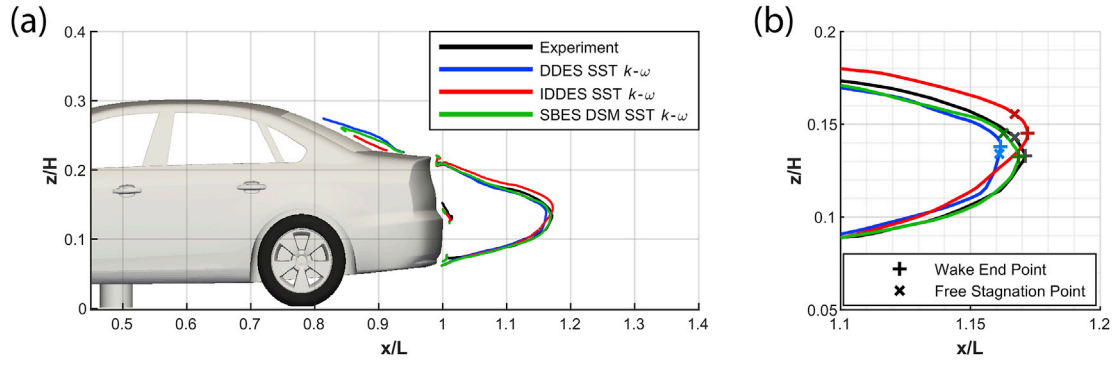
Fig. 6. Rear wake for the Notchback model at 0° yaw for the measurements and simulations. In (a), the wake isoline ($u = 0$) is seen for the rear of the vehicle. No experimental data exist for the separation region over the rear window. A close up of the most downstream part of the wake is seen in (b) and includes the position of the wake endpoint and free stagnation point.
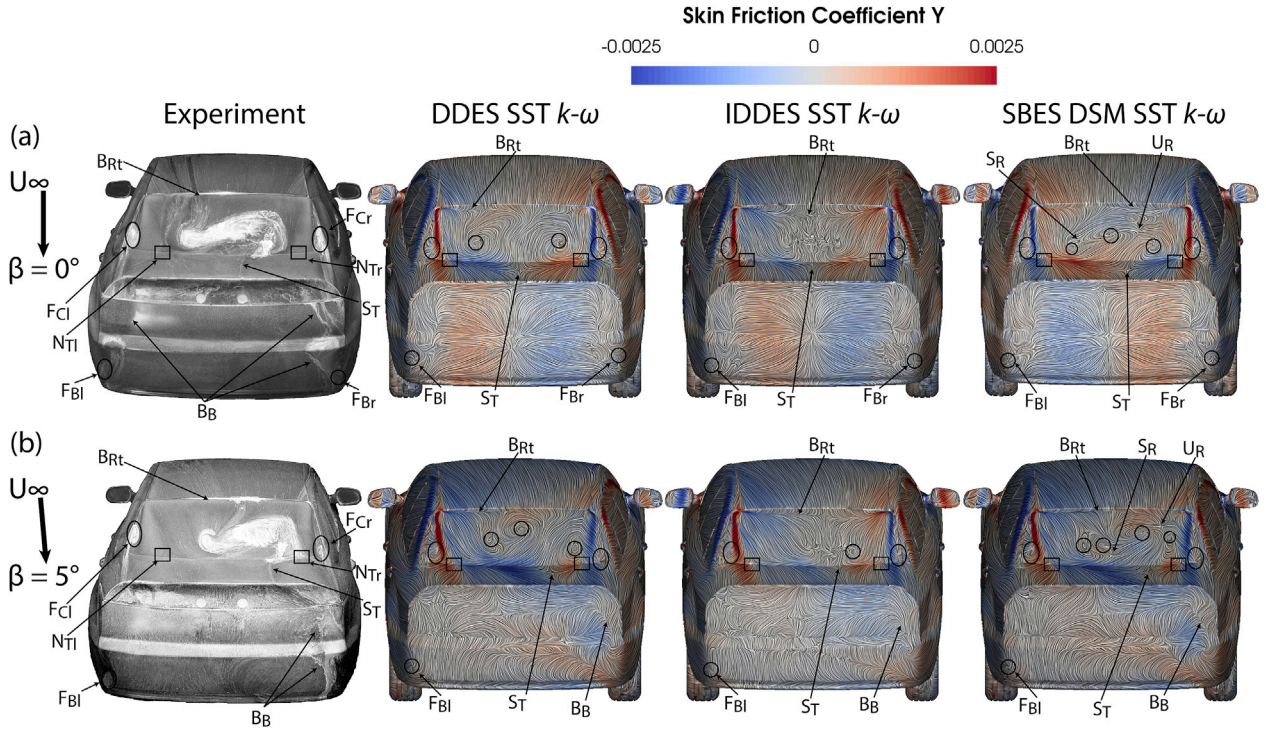

Fig. 7. Near-wall flow behavior for the notchback configuration at 0° (a) and 5° (b) yaw, for the experiment and the hybrid RANS-LES models. The oil film is used for the experimental visualization. The simulation results are colored with the time-averaged spanwise skin friction coefficient for easier identification of near-wall flow structures. The most dominating skin-friction structures are notated, where focus points are notated with F and circles, unstable nodes with U, saddle points with S, and bifurcation lines with B.

The asymmetrical separation bubble is neither captured by the DDES nor the IDDES models, as both models predict symmetric behavior over the rear part of the body. Even when trying to trigger asymmetrical flow over the rear window by increasing the yaw angle to 1°, no significant change occurs of the near-wall flow for the DDES and IDDES models. This is due to the DDES model overpredicts the separation at the central section of the rear window, giving rise to the two counter-rotating focis, notated by circles in Fig. 7 panel a. The opposite behavior is seen for the IDDES model, as only a small separation is seen directly at the beginning of the rear window together with a small recirculation region at the rear window and trunk intersection. In the measurements, a small shallow separation over the central section of the rear window results in reversed flow for the top central region, causing the bifurcation line (B_{Rt}), Fig. 7 panel a.

At the C-pillars inside the bifurcation lines, stable focus points (circles) on the left (F_{Cl} and right F_{Cr}) sides are seen, similarly captured by

the RANS-LES models. A saddle point (S_T) appear slightly to the right of the middle of the trunk in the experiment, caused by the reversed flow over the central section of the rear window, Fig. 7 panel a. The hybrid RANS-LES models capture this saddle point but for different positions, as it depends on the flow over the central section of the rear window. The SBES model predicts the saddle points position similar to the experiment, slightly east of the car symmetry line ($y = 0$). A similar pattern and position of a saddle point are also seen on the trunk of the notchback car body in a similar flow condition Gaylard et al. (2007).

Fewer structures are seen at the base for the oil film visualization of the notchback configuration at 0° yaw (Fig. 7 panel a). Two focus points (F_{Bl} and F_{Br}) can be seen at the lower sides of the base, caused by the separation at the edge of the base. These stable focus points are well captured by the simulations and are the sources for the lower pressure and pressure fluctuations seen for these regions in Figs. 9 and 11. The DDES and SBES models predict similar behavior for the near-wall flow of
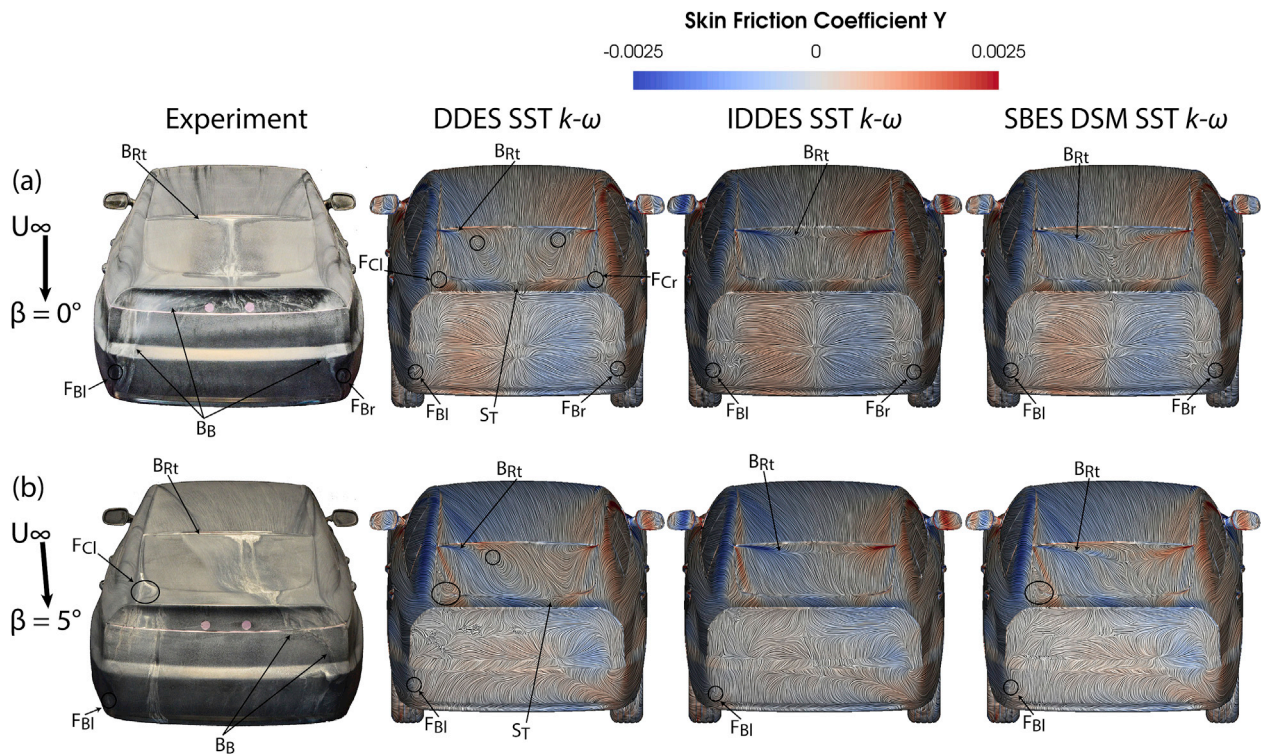
Fig. 8. Near-wall flow behavior for the fastback configuration at 0° (a) and 5° (b) yaw, for the experiment and the hybrid RANS-LES models. The oil film is used for the experimental visualization. The simulation results are colored with the time-averaged spanwise skin-friction coefficient for easier identification of near-wall flow structures. The most dominating skin friction structures are notated. For an explanation of notations, see caption in Fig. 7.

the base, with two unstable node points just above and below the central part of the bumper. The unstable node below the bumper is caused by the two large spanwise vortices dominating the wake Strangfeld et al. (2013), Wieser et al. (2015a), while the corner of the bumper causes the one just above the bumper. Only the unstable node above the bumper occurs for the IDDES model, as an effect of the slightly upward shifted wake, seen in Fig. 6. Some streaks of oil film can be seen for the sides of the base in the experiments (B_B); these coincide well with the outer bifurcation lines caused by the rear wake spanwise vortical structures, seen in the simulations.
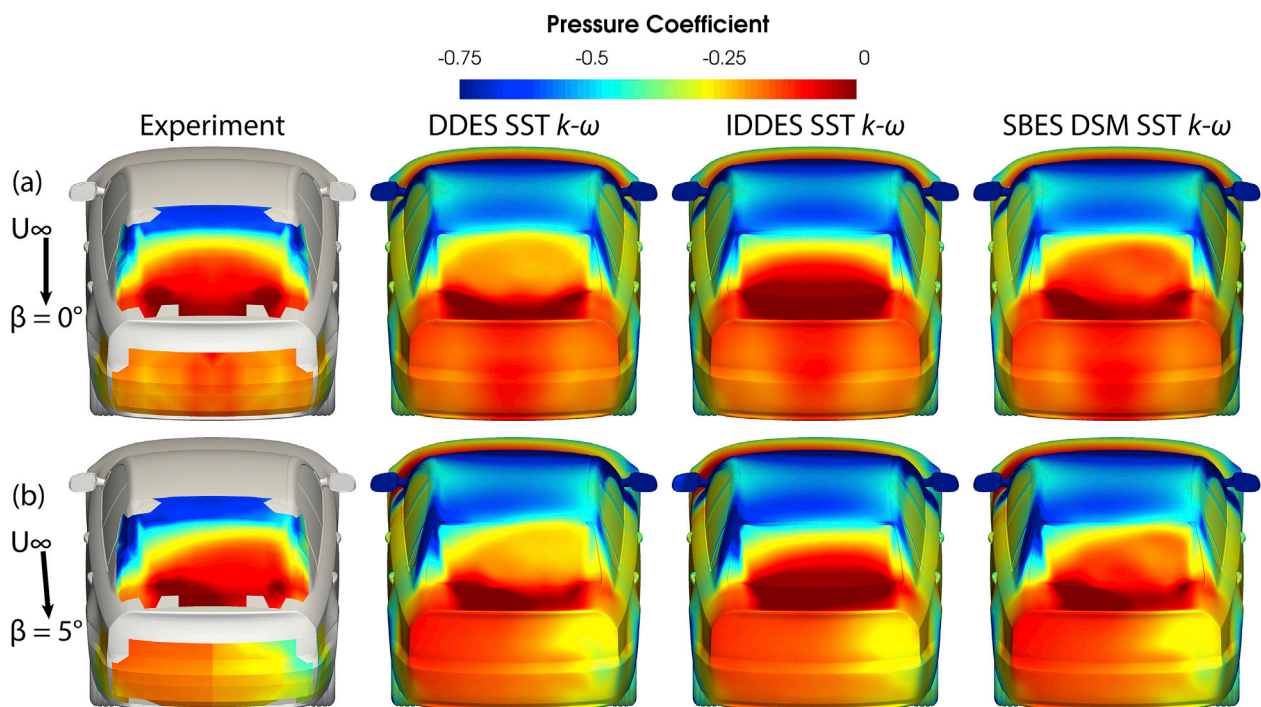

Fig. 9. Time-averaged pressure coefficient at the rear part of the notchback configuration at 0° (a) and 5° (b) yaw, for the experiment and the hybrid RANS-LES models.

For 5° yaw, Fig. 7 panel b, the recirculation region over the rear window has shifted towards the leeward side and reduced in width, while more attached flow occurs over the windward side. The central section is still dominated by the large separation bubble at 5° yaw. However, the most western region of it now consists of two rotating structures. The width of the circulation region is seen to be limited by the leeward side A-pillar vortex in the experimental visualization, as a clear oil film path is seen between the circulation region and the leeward C-pillar, compressing the effect of the right C-pillar focus point F_{Cr}. For the saddle point on the trunk, S_T, a clear leeward shift is seen (compared to 0° yaw) in the experiment, caused by this leeward A-pillar vortex interaction.

The SBES models resemble this behavior well, as the stable focus points are located in the regions where dense oil film is seen in the experiment. For the SBES model, the saddle point S_R and unsteady node U_R are still present here but have shifted its position to the leeward side compared to 0° yaw. The DDES model captures parts of the behavior seen in the measurement, as two rotating focis exist at the central section of the rear window. However, too strong upstream flow at the rear window mid-section, caused by the overpredicted separation removes the possibility of capturing other near-wall structures. Over-attached flow is again seen for the IDDES model, resulting in a too-small recirculation region at the central section of the rear window. Only minor differences are seen between the hybrid RANS-LES models for the near-wall flow of the base at 5° yaw, as they predict similar flow in the wake, Fig. 7 panel b. Only the left stable focus point (F_{Bl}) is visible at the lower part of the bumper in the experiments. Indications of the bifurcation lines B_B caused by the counter-rotating vortices in the wake exist for the leeward side of the base in the experiments and is also seen in the simulations. Some curved streaks of oil film are also seen for the central section of the bumper, as seen for the DDES and SBES models.

In Fig. 8, the near-wall flow behavior for the fastback configuration is seen for the experimental oil film visualization and simulations. In the experimental visualization at 0° yaw (Fig. 8 panel a), a dense region of oil film is seen at the central section of the rear window, indicating flow moving towards the car symmetry line ($y = 0$) Wieser et al. (2014). This results in a less complex flow behavior over the rear window, compared to the notchback configuration, with no asymmetric recirculation region. A small separation is seen, at the central section of the beginning of the rear window in the experiment, resulting in the bifurcation line (B_{Rt}). This bifurcation line is only seen near the top corners of the rear window for the DDES model, as it as well here overpredicts the separation, resulting in reversed flow over the central section of the rear window and two stable focis (circles). This causes substantial inflow towards the central section of the lower part of the rear window and generates two stable focus points (F_{Cl} and F_{Cr}) near the C-pillars and also the saddle point (S_T) on the trunk. Neither of these stable focis nor the saddle point is seen in the experiment nor for the other two hybrid RANS-LES models. The IDDES model is most aligned with the experiment, as it predicts the smallest separation at the top of the rear window. The SBES model predicts similar behavior, but with a too large separation and less uniform near-wall flow at the central section.

The visible oil film traces the base, seen in the experiment for the fastback configuration (Fig. 8 panel a), are similar to the behavior seen for the notchback configuration at 0° yaw. The two stable focus points (F_{Bl} and F_{Br}) at the lower part of the bumper are present, and traces of spanwise flow (B_B) is seen at the top part of the central section of the base. However, these latter traces might be significantly affected by gravity, so their direction cannot be determined with full certainty. Similar to the notchback configuration, some bifurcation lines (B_B) are seen near the sides of the base. Here very similar behavior of the skin friction lines is seen between the hybrid RANS-LES models, indicating that the near wake behavior is relatively insensitive to the flow over the rear window. The models capture the two rotating focus points (F_{Bl} and F_{Br}) and the bifurcation lines B_B formed by the vortices in the wake.

For 5° yaw, the dense region of oil film is directed towards the

leeward side of the fastback configuration, Fig. 8 panel b. Only a small separation exists on the beginning of the rear window forming the bifurcation line B_{Rt}. Both the IDDES and SBES models capture this separation, although overpredicted, especially by the SBES model. The DDES model repeatedly overpredicts the separation over the rear window, resulting in a stable focus point (circle) and the saddle point (S_T) on the trunk. On the windward side of the trunk, near the end of the C-pillar, an indication of a focus point is seen in the experiment (circle), caused by the stronger spanwise flow over the lower part of the rear window compared to 0° yaw. Both the DDES and SBES models capture this focus point, as a small separation occurs at the windward C-pillar.

No significant difference for the oil film traces on base is seen for the fastback configuration when compared to the notchback configuration at 5° yaw, Fig. 8 panel b. Here, the hybrid RANS-LES models are similar, except for some minor differences at the top windward part of the base for the DDES model. In this region, vertical ridges of oil film are seen in the experiments, which both the IDDES and SBES models capture well. For the top leeward side corner of the base, curved behavior of the oil film streaks are seen, indicating the bifurcation lines B_B formed by the flow in the wake, well agreeing with what is seen in the simulations.

Worth noting is the distinct difference of the near wake of the mirrors occur for the IDDES model, compared to the DDES and SBES models, as the vertical bifurcation lines are located further outwards. Unfortunately, no experimental visualization exists for this region of the car configurations.

3.4. Rear-end pressure distribution

As significant differences of the near-wall flow over the rear part of the vehicles are seen between the hybrid RANS-LES models and measurement, it is of interest to see the effects on the surface pressure.

In Fig. 9 panel a, the pressure distribution at the rear of the notchback is seen for 0° for both the measurement and simulations. A gradual increase of pressure is seen on the top rear part of the body, as the flow is exposed to expansion, caused by the slanting roofline, with the maximum pressure ($C_P = 0.1$) occur at the trunk. Worth noting is that detailed pressure measurement is only performed on half the car body and therefore mirrored around the car symmetry line ($y = 0$) for 0° yaw, resulting in symmetric pressure distribution. This symmetry is not expected at 0° yaw, as an asymmetric separation bubble exists at the rear window for the notchback, Fig. 7. This pressure increase is captured differently between the hybrid RANS-LES models, due to their differently predicted separations over the rear window. The overpredicted separation causes the DDES model to fail to capture the gradual pressure increase over the rear window, being the reason for the higher drag and lift forces than seen for the other models. However, the pressure distribution at the trunk is similar to the measurement, as the separation not cover the trunk. The IDDES model overpredicts the high-pressure region at the rear window and on the trunk as a result of the smaller recirculation region seen in Fig. 7 panel a. The SBES model aligns well with the measurement, albeit slightly lower, and asymmetric pressure distribution is seen at the rear window's central section. In the measurement, a pressure increase is seen in the top corner of the rear window, which is caused by interpolation of the pressure distribution Wieser et al. (2014).

The pressure at the base is captured similarly for the RANS-LES models and consist well with the measurement at 0° yaw, Fig. 9 panel a. Lower pressure is seen at the sides of the base with its center near the B_B bifurcation lines (seen in Fig. 7 panel a). Slightly lower pressure at the lower part of the central section of the bumper is seen for the IDDES model, as an effect of the more upward shifted wake, Fig. 6.

For 5° yaw, the increased pressure at the rear window is moved to the leeward side, Fig. 9 panel b. The higher pressure seen on the trunk is, however, shifted in the opposite direction, as a broader high-pressure region is seen on the trunk's windward side. The SBES model agrees well with this behavior, which is seen in the measurement. The DDES model captures the correct pressure distribution on the trunk while

missing the increased pressure on the rear window, caused by the over-predicted separation at the rear window, resulting in higher drag and lift. Meaning that the good correlation to the measured lift force at 5° yaw is a coincident rather than correctly captured flow field. The higher pressure on the leeward side of the trunk is reduced with the yaw increase, as the effect of both the leeward side A-pillar and C-pillar vortices are pushed further out from the central section of the vehicle, resulting in less high energy flow hitting the trunk. The IDDES model overpredicts, as seen for 0° yaw, the pressure seen on the lower part of the rear window and the trunk.

At 5° yaw, a low-pressure region is developing on the leeward side of the base in the measurement, Fig. 9 panel b. The hybrid RANS-LES models capture this and its shape well, and no significant differences are seen between the models. However, slightly lower pressure is seen in the measurement, especially for the top leeward corner. Lower pressure also occurs at the bottom windward corner of the base due to the presence of the F_{Bl} stable focal point, seen in Fig. 7 panel b, well captured by the hybrid RANS-LES models.

The excellent correlation to the measured drag of the notchback for the SBES model is mainly due to the model that can capture the behavior of the pressure increase over the rear of the vehicle, especially at the rear window. Higher drag, compared to the SBES model, is seen throughout the yaw sweep for the DDES model, mainly due to the lower pressure distribution at the rear window. This lower pressure is also the reason for the higher lift force than seen for the other models, which make it correlate better to the measured absolute value. For the IDDES model, the broader region of higher pressure at the rear window and trunk is the leading cause of the lower drag and lift forces for the whole yaw sweep.

Higher pressure, compared to the notchback, is seen at the end of the roof for the fastback car configuration at 0° yaw in the measurement, Fig. 10 panel a. The lower roof decline results in longer C-pillars, generating a more triangle-shaped pressure increase at the rear window, compared to the notchback configuration. Both the IDDES and SBES models capture this high-pressure distribution. However, with too low pressure at the beginning of the rear window, especially for the SBES models, caused by the overpredicted separation. Similar to the notchback configuration, the DDES model underpredicts the pressure at the rear

window. As for the notchback configuration, high pressure ($C_P = 0.1$), caused by the momentum of the A-pillar vortices, occurs on the trunk of the fastback in the measurement. Here, the DDES model is predicting similar pressure distribution, as seen in the measurement. Both the IDDES and SBES models overpredict the high-pressure region, despite capturing the near-wall flow behavior seen in the experiment.

As for the near-wall flow of the base, no significant difference of the base pressure is seen when comparing the notchback and fastback car configurations, neither for the measurements nor simulations. Generally, a slightly lower base pressure occurs in the measurement, which explains the higher measured drag than in the simulations.

For 5° yaw, the pressure increase on the rear window of the fastback configuration is shifted towards the leeward side, Fig. 10 panel b. The opposite occurs for the high pressure on the trunk in the measurement, also seen for the notchback, where the higher pressure is concentrated at the windward side. Both the DDES and SBES models capture this shift of high pressure on the trunk. It should be noted that the pressure probe grid used in the measurement is coarse at the trunk and that the shape of the measured high-pressure region might not be accurately captured. No significant difference to the base pressure seen for the notchback at 5° yaw is seen neither for the measurement or simulations.

Similar to the notchback, the lower pressure at the rear window of the fastback causes the DDES model to predict higher drag and lift forces than seen for the IDDES and SBES models. The lower predicted lift force for fastback configuration for the IDDES model is a result of the over-predicted high-pressure region on the trunk and bottom part of the rear window.

The flow around cars and other ground vehicles rarely behave steady, and the DrivAer car bodies are no exceptions. The unsteady flow result in pressure fluctuations and are hence investigated for the rear part of the DrivAer configurations, Figs. 11 and 12.

For the notchback body at 0° yaw, high-pressure fluctuations ($C_p \leq 0.05$) occur around the C-pillars and on the trunk in the measurement, Fig. 11 panel a. The pressure fluctuations inside of the C-pillars are seen where the rotating focis F_{Cl} and F_{Cr} are present. Inside of the C-pillars, fluctuating pressure is also seen from the paths of the C-pillar vortices. Outside of the C-pillars, some pressure fluctuations are also
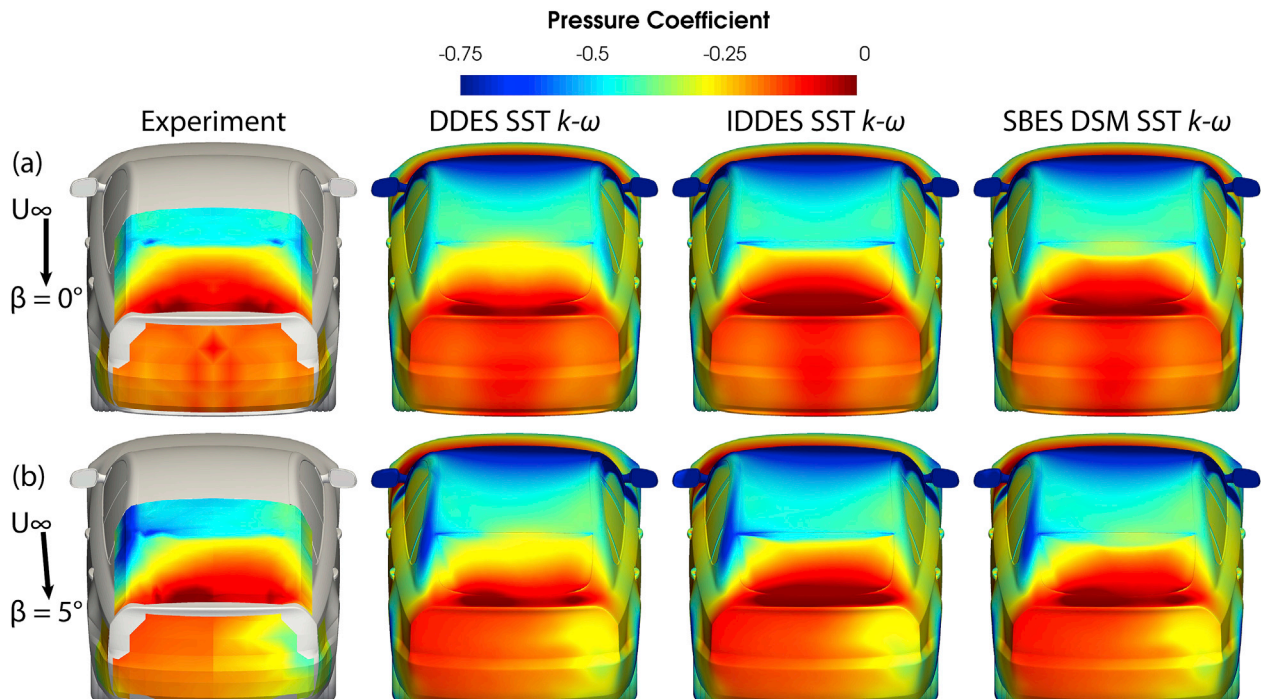

Fig. 10. Time-averaged pressure coefficient at the rear part of the fastback configuration at 0° (a) and 5° (b) yaw, for the experiment and the hybrid RANS-LES models.
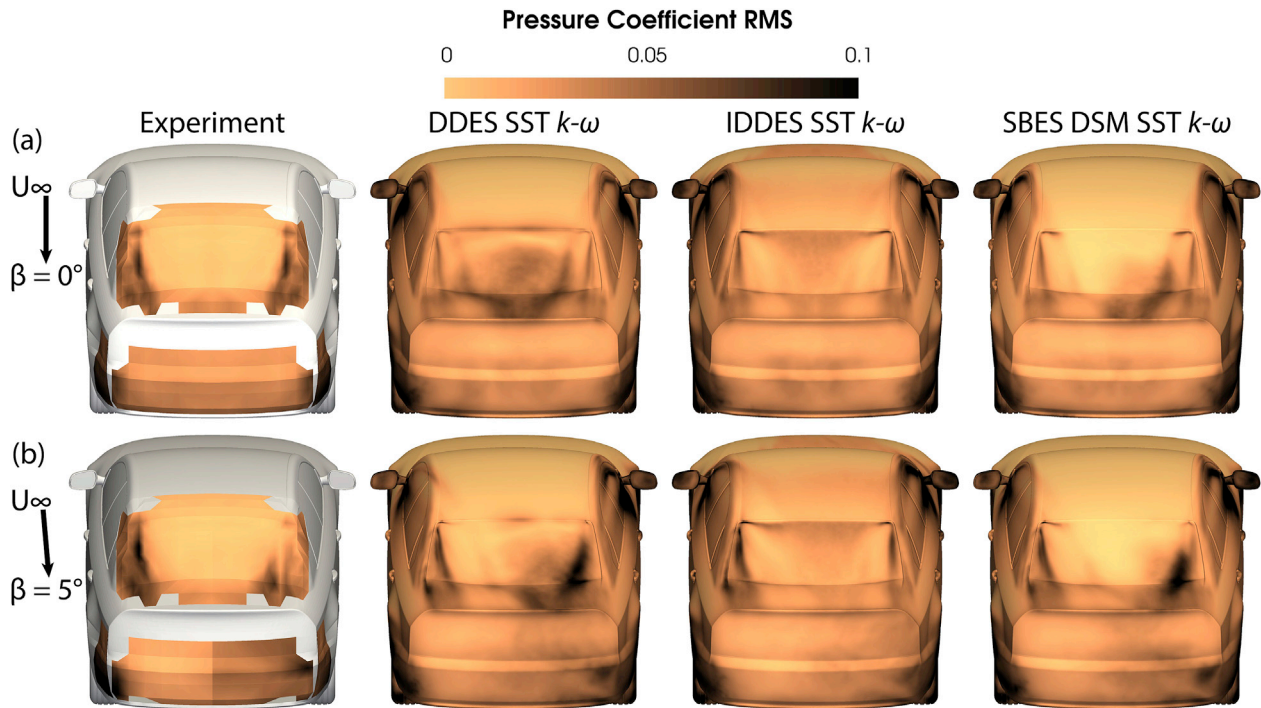
Fig. 11. Normalized time-averaged pressure fluctuations at the rear part of the notchback configuration at 0° (a) and 5° (b) yaw, for the experiment and the hybrid RANS-LES models.
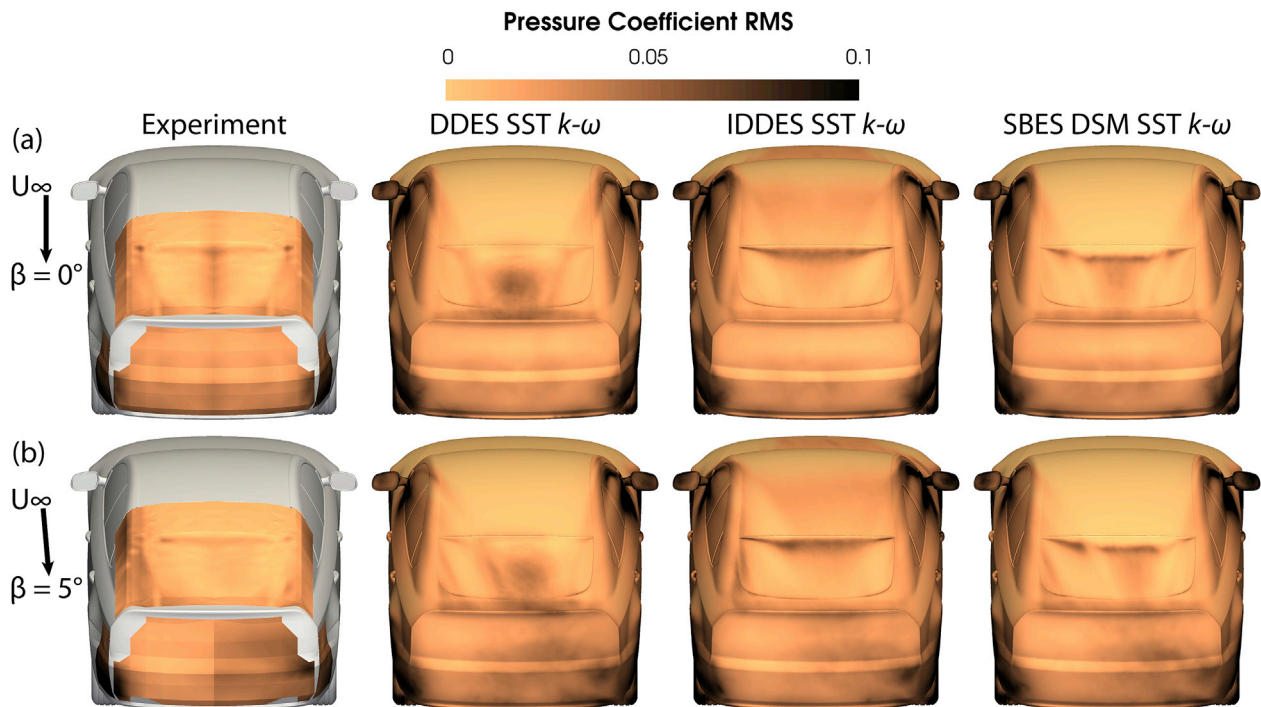

Fig. 12. Normalized time-averaged pressure fluctuations at the rear part of the fastback configuration at 0° (a) and 5° (b) yaw, for the experiment and the hybrid RANS-LES models.

seen, caused by the unsteady flow from the mirrors upstream. Symmetrical behavior of the pressure fluctuations is seen in the measurement, due to only one-sided measurements. Asymmetric pressure fluctuations may be expected over the rear window, as seen for the SBES model, where fluctuations are seen for the right side of the rear window.

The hybrid RANS-LES models capture the pressure fluctuations around the C-pillars at 0° yaw, Fig. 11 panel a. However, more extensive regions of fluctuations are seen in the measurement, possibly due to the pressure probe distribution. For the central section at the rear window, significant differences between the three hybrid RANS-LES models occur. The large separation seen for the DDES model results in severe unsteadiness and pressure fluctuations at the central section of the rear window, where no or low fluctuations are seen in the measurements. For the IDDES model, pressure fluctuations are mainly seen from the

separated flow at the top of the rear window. High-pressure fluctuations are also seen at the wheel arches behind the rear wheels in the measurement (Fig. 11 panel a), caused by the separating flow over the rear wheels. These pressure fluctuations extend to the lower sides of the base, where the stable focus points F_{Bl} and F_{Br} are present. The hybrid RANS-LES models capture these pressure fluctuations at the rear wheel arches and how it extends to the lower sides of the base.

For 5° yaw, the region of pressure fluctuations around the windward C-pillar is increased in size in the measurement (Fig. 11 panel b), as separation occurs at the C-pillar. The hybrid RANS-LES models capture this well, and also how it propagates downstream onto the trunk's windward side. For the leeward side of the rear window, pressure fluctuations are located in a concentrated region, a region affected by the leeward side A-pillar and C-pillar vortices. Both the DDES and SBES models align well with the measurement for this region, and both models predict a focus point in this region. The IDDES model fails to replicate the measured pressure fluctuations on the leeward side of the rear window. Pressure fluctuations on the base surface are mostly concentrated on the leeward side of the base in the measurement, Fig. 11 panel b. These fluctuations comply with the region where the lower surface pressure is seen, Fig. 9. The hybrid RANS-LES models agree well with the measured pressure fluctuations. Only small differences between the models are observed, as slightly lower pressure fluctuations occur for the IDDES model. Higher levels of pressure fluctuations are seen for the lower part of the windward side wheel arch, compared to the leeward side, as less attached flow occurs on the leeward side.

Much lower pressure fluctuations over the rear window than the notchback configuration, are seen for the fastback configuration, Fig. 12.

For 0° yaw, only low-pressure fluctuations are seen in the measurement around the C-pillars, the central section of the rear window and at the trunk, Fig. 12 panel a. The pressure fluctuations at the central section of the rear window coincide well with dense regions of the oil film in the experiment (Fig. 8 panel a). The lower pressure fluctuations around the C-pillars are also seen in the simulations. However, significant differences are seen for the central section of the rear window. Here, the DDES model overpredicted separation leads to too high pressure fluctuations on the lower section of the rear window and at the trunk. The IDDES and SBES models are more aligned with the measurement, as the pressure fluctuations are concentrated to the top and middle section of the rear window. The slightly overpredicted separation at the beginning of the rear window forces the pressure fluctuations downstream further than seen in the measurement. The pressure fluctuations on the wheel arches and lower sides of the base are similar to what is seen for the notchback configuration (Fig. 11 panel a), suggesting low sensitivity of the rear-end configuration.

For 5° yaw, lower pressure fluctuations are seen at the central and leeward section of the rear window, Fig. 12 panel b. The pressure fluctuations for the windward C-pillar and the windward side of the trunk are well captured in the simulations. The overpredicted separation for the DDES model still results in too high pressure fluctuations at the center of the rear window. In contrast, the IDDES and SBES models comply well with the measurement. The overprediction of the separation at the rear window for the DDES model results in more unsteady behavior over the central part of the rear window and trunk, which transfers into the wake and causes higher pressure fluctuations for the central section of the base.

3.5. Differentiating behaviors of the hybrid RANS-LES models

Significant differences are seen between the hybrid RANS-LES models, even though they are based on the same strategy of modeling and resolving the turbulence in different regions, showing the importance of it.

The IDDES and SBES models have the ability to switch from RANS to WMLES mode for the near-wall region, if enough upstream turbulence exists, resulting in more resolved turbulence near the wall. The effect of the WMLES mode in the IDDES model is seen in Figs. 11 and 12, as small

pressure fluctuations are seen on the hood and roof, which is not seen for the DDES and SBES models.

To investigate the switch from RANS to WMLES further, the coherent turbulent structures (Q-criterion) colored with the turbulent viscosity ratio, ν_t/ν, are seen for the notchback configuration at 5° yaw in Fig. 13. The investigated models resolve turbulent structures in the regions where the separated flow is expected, e.g., from the wheels, mirror, A-pillars, C-pillars, rear window, and the base. However, the IDDES model also resolve turbulent structures at the hood and roof. This is not seen for the DDES and SBES models, where turbulent structures only are seen for regions with flow separation, and confirms that the IDDES model acts in WMLES modes for these regions. From the coherent turbulent structures, it is seen that the small separation occurring at the grill is enough to trigger the IDDES model into WMLES mode. This separation is captured by all models, as small turbulent structures are resolved directly downstream of the grill, but it is not enough to trigger the SBES model into WMLES mode. For seeing if this is a typical IDDES model behavior, the IDDES model with the Spalart-Allmaras RANS model is included. Similar to the DDES and SBES models, the IDDES SA model does not resolve any turbulent structures on the hood and roof, even though similar separation is seen from the grill, Fig. 13. This indicates that the IDDES model with the SST $k - \omega$ RANS model earlier switches to WMLES than with the SA RANS model.

Although more resolved turbulence may seem favorable, it may, unfortunately, lower the accuracy if it is not sufficiently resolved. In this study, the early switch to WMLES causes some drawbacks, as significantly lower skin friction than the other models is seen at the bonnet and roof for the IDDES model, Fig. 14. This is most likely an unphysical behavior, as the flow over the bonnet resembles flow over the top of an airfoil, where RANS models accurately predict skin friction Catalano and Tognaccini (2011), Aranake et al. (2015). The reason for the lower skin friction seen in this study is that a too coarse grid is used in the near-wall region for sufficient WMLES, as under-resolved turbulent stresses result in too low skin friction. This shows that the IDDES SST model can, under certain conditions, prematurely switch to WMLES mode when the RANS mode would be sufficiently accurate. This is a drawback for the IDDES model, especially when using the SST $k - \omega$ RANS model, as the need for a finer grid for accurate WMLES behavior causes the model to be much more expensive than the other models. It also makes the IDDES model more difficult to use than the DDES and SBES models, as the user needs to know which mode the model will use for the near-wall region to ensure sufficient grid resolution.

One of the significant challenges with hybrid RANS-LES models is to be able to transit rapidly between the RANS and LES regions. A slow transition leads to a sort of pseudo-laminar-turbulent transition to occur, leading to losses of resolved stresses and too low turbulence levels before fully developed resolved turbulence is achieved further downstream Mockett (2009), Spalart et al. (2006), Sagaut (2013). Rapid transition is especially important for separating shear layers, where a slow transition can result in a longer separation than might be expected, and is a typical problem for the DDES and IDDES models Menter (2016). The shielding function in SBES enables a more aggressive definition of the LES length scale for faster (than DDES) transition between the RANS and LES regions. This results in reduced the turbulent viscosity ratio for the LES region, which makes it possible for the model to resolve more turbulent structures. This is seen in Fig. 13, where significantly lower (around half) turbulent viscosity for the coherent turbulent structures is seen for the SBES compared to the other models. Leading to more and also smaller resolved coherent turbulent structures for the SBES model, compared to the other models, is seen for the wakes of the mirrors and the A-pillar vortices.

Overall similar skin friction is seen between the DDES, SBES, and IDDES SA models, as they mostly operate in RANS mode for the near-wall, Fig. 14. At the bottom lip of the front, the DDES and IDDES SA models predict a significantly larger separation than seen for the SBES and IDDES model, even though the DDES model uses the same RANS
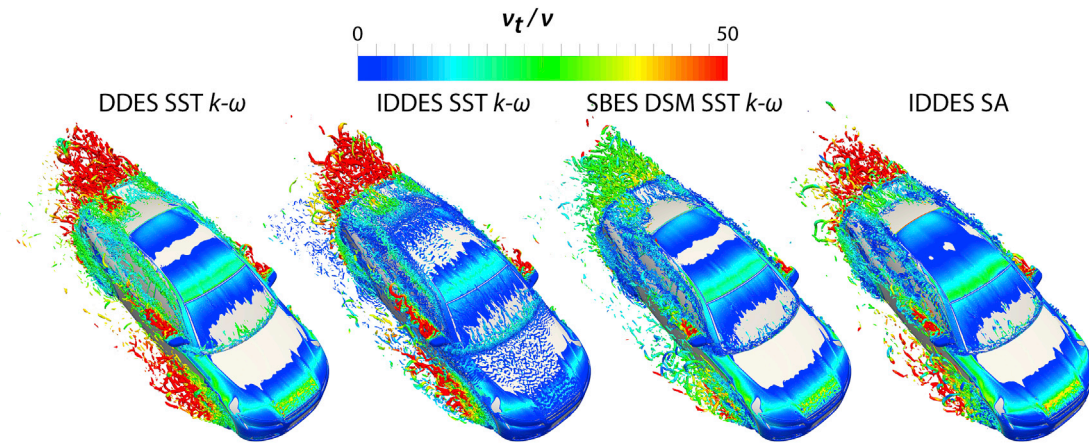
Fig. 13. Coherent turbulent structures ($Q = 3 \cdot 10^6$ s^{-2}) colored with the eddy viscosity ratio for the notchback configuration at 5° yaw, for the DDES, IDDES, SBES, and IDDES SA models.
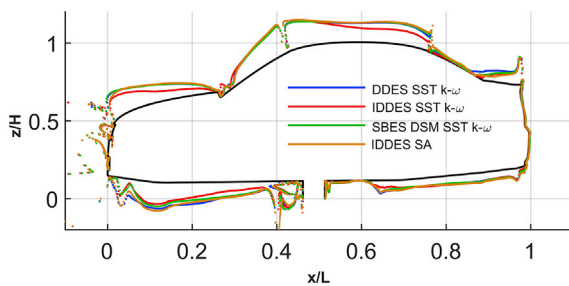

Fig. 14. Skin friction magnitude showed as the distance from the surface of the notchback body in the $y = 0$ plane for 5° yaw. Note the significant lower skin friction for the IDDES model with the $k - \omega$ SST model.

model ($k - \omega$ SST) as the SBES and IDDES models. This larger separation for the DDES and IDDES SA models is caused by the slower transition between the RANS and LES regions than for the SBES model, leading to lower resolved stresses at the beginning of the separating shear layer and thereby a later reattachment of the flow. Here, the IDDES model predicts similar behavior as the SBES model, as it acts in WMLES mode just upstream the lip (caused by the lower grill opening) and therefore is already resolving turbulent structures near the wall, leading to resolved stresses at the beginning for the separating flow. This, together with a fine grid resolution over the lower part of the bumper, to ensure a good geometrical representation of the small radii on the front lip, leads to well-resolved structures for the WMLES in the IDDES model.

In Fig. 15, the velocity profile, turbulent viscosity ratio, and resolved TKE are shown for four lines along the notchback body at 5° yaw for the DDES, IDDES, and SBES models. For line (a), located at the center of the bonnet, significantly lower near-wall velocity is seen for the IDDES model, compared to the DDES and SBES models. The lower near-wall velocity is an effect of under resolved turbulent stresses in the near-wall region caused by the WMLES mode of the IDDES model, as the grid is too coarse for it. The under-resolved stresses result in too low skin friction, as seen in Fig. 14, but also a slightly thinner boundary layer compared to the DDES and SBES models. The DDES and SBES models behave equally for this region of the attached flow, as both are in RANS mode as no resolved TKE occurs.

For line (b), located directly upstream the rear window, the behavior as for line (a) is still present. Much lower turbulent viscosity is seen for the IDDES model, as it is in WMLES mode. However, a crucial difference for the resolved TKE is seen between the DDES and SBES models, as the DDES model resolves some TKE in the near-wall region. Upstream the rear window, a steadily behaving boundary layer is present, which both the DDES and SBES models mainly solve in RANS mode, as expected from

the models. However, a curved list connects the roof to the rear window, and the grid is refined for sufficient representation of the curvature, Fig. 2 panel b. This grid refinement is an issue for the DDES model, which, despite its reasonably strong shielding of the RANS region, cannot sufficiently shield the RANS region in this region. This is due to the boundary layer thickness just upstream of the rear window is 6.54 mm (equal to $18.6 \cdot 10^{-3} H$) for the DDES model, while the maximum grid edge size in this region is between 1.3 and 0.5 mm. As the shielding function in the DDES model is based on the max cell edge length, this results in that more than five cell edge lengths cover the boundary layer thickness, which is enough for the RANS shielding in DDES to breakdown Menter (2016). This means that the LES mode in the DDES model is active within the boundary layer just upstream of the rear window, resulting in under-resolved stresses as the grid is too coarse for wall resolved LES. The effect of this is also seen for the lower skin friction for the DDES model, compared to the SBES and IDDES SA models, upstream the rear window, Fig. 14. This lack of sufficient shielding is the main reason for the overpredicted separations over the rear window for the DDES model. The IDDES model has, as well here, a slightly thinner boundary layer ($\approx$ 5% thinner than for the DDES and SBES models) upstream the rear window, compared to the DDES and SBES models. This results in more high energy flow closer to the wall, and as the model is in WMLES mode, resolved turbulence already exists. Although the resolved stresses might be lower than expected on a WMLES suitable grid, the higher energy flow, together with the reasonably resolved turbulence results in the smaller separation over the rear window. The shielding function in the SBES model is not affected by this grid refinement, and the model's ability to rapidly switch from RANS to LES results in the intermediate separation compared to the DDES and IDDES models.

At line (c), positioned at the end of the trunk, the velocity and resolved TKE are dependent on how the models predict the flow over the rear window, as significantly more resolved TKE occurs for the DDES model. Near the wall, similar behavior for the velocity is seen, while further away from the wall, less momentum is seen for the DDES model, due to its larger recirculation region. The SBES model also resolves a significant amount of TKE but maintains the viscosity ratio between two and four times lower than seen for the IDDES and DDES models, allowing for smaller resolved turbulence structures. In the wake, line (d), the models predict similar velocity distribution, and the slightly upward shifted wake for the IDDES model, results in less resolved TKE in the lower part of the wake.

4. Conclusions

The flow around the DrivAer reference model is investigated with three hybrid RANS-LES models, the DDES, IDDES, and SBES models. The
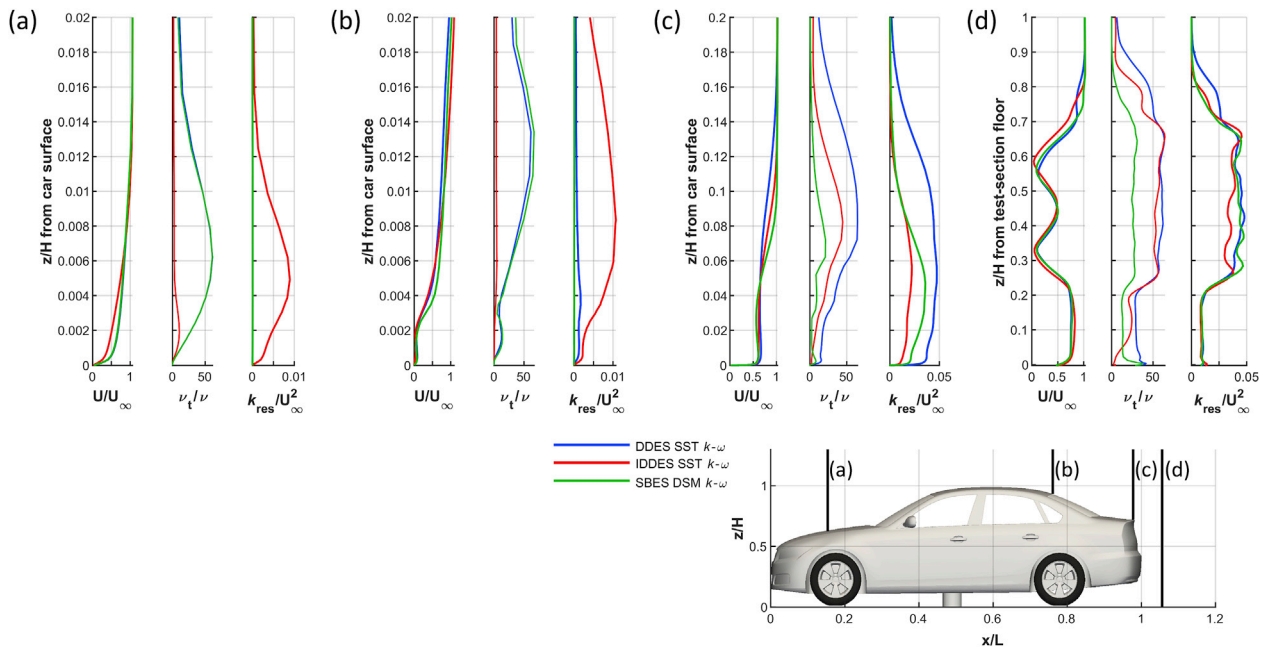
Fig. 15. Normalized velocity magnitude, eddy viscosity ratio and normalized resolved turbulent kinetic energy for the investigated hybrid RANS-LES models for four lines located at the bonnet (a), roof (b), trunk (c) and in the rear wake (d) of the notchback configuration at 5° yaw.

models are investigated for both the notchback and fastback car configurations over a range of yaw angles and compared to wind tunnel measurements. A large section of the wind tunnel is included in the simulation domain for a fair comparison to the wind tunnel measurements.

The hybrid RANS-LES models are generally in close agreement with the absolute measured aerodynamic forces. For the notchback body, the best correlation to the measured drag force over the yaw sweep, consisting of five yaw angles, is seen for the SBES model. Both the DDES and IDDES models agree well with the measurements for certain yaw angles but are not consistent over the yaw sweep. For the fastback body, investigated for two yaw angles, the best correlation to the measured drag force is seen for the DDES model. Here, the SBES and IDDES models underpredict the drag force, compared to the DDES model and the measurements. The DDES model captures the absolute lift force best for the two bodies, while too low lift force is seen for both the SBES and DDES models, particularly for the fastback body.

Predicting the absolute measured forces is important, but slight differences in the body set-up or flow conditions might cause significant differences between the measurement and simulations. Less sensitive to the set-up and arguably more crucial during aerodynamic development of vehicles is to achieve high accuracy of the force changes caused by changed flow conditions or geometrical differences. The latter being particularly important with the introduction of the WLTP legislation, as all small changes might affect the fuel consumption and hence emissions. The SBES model achieves excellent correlation to the measured changed drag force when increasing the yaw angle, as less than 2 drag counts difference is seen for the two car bodies. Less consistent agreement to the measurement is seen for the DDES and IDDES models, predicting the incorrect sign of the drag change for certain yaw angles. For the changes of lift force with increased yaw angle, all the modes struggle for the lower yaw angles ($\leq 2°$), while the IDDES and SBES models are close to the measured lift change for the larger yaw angles.

The SBES model can pick up the small trends seen for changes in flow conditions and geometry, making it highly accurate and reliable for predicting the aerodynamic drag for cars. The main reason for predicting the forces so consistently is the model's ability to predict the complex flow over the rear windows of the car configurations. This is particularly seen for the notchback configuration, which has a complex asymmetric

separation over the rear window, which the SBES model is the only model to capture accurately. The IDDES model is in the best agreement with the measurements for the flow over the fastback body's rear window. However, the SBES model is not far off as it captures the correct behavior with only the wrong magnitude of some features.

The hybrid RANS-LES models investigated in this study are all based on the same approach of using RANS for the near-wall region and LES further away from the wall. The IDDES and SBES models can also, if enough unsteadiness exists upstream, use WMLES for the near-wall region. How these models switch between the RANS and LES regions, and the WMLES mode is seen to cause significant differences in the results. The IDDES model is seen to switch to WMLES mode prematurely, triggered by small separations. This can results in incorrect behavior of the near-wall flow, as too low skin friction and thinner boundary layer than expected is seen in this study, significantly affecting the flow over the rear of the car bodies. Typical hybrid RANS-LES meshes are not suited for WMLES, where developed boundary layers are expected, as the original idea of the WMLES is to keep the unsteadiness in the near-wall region in recirculation regions. This makes the IDDES model more difficult to use, as the user needs to be aware of which mode the model will be acting in, which might be difficult to know prior to the simulation. To ensure sufficiently resolved WMLES in developed boundary layers, a significantly finer grid is required, which greatly will increase the computational cost.

The SBES model offers a more rapid switch from the RANS to LES region than the other two models, being especially important for accurate prediction of separation shear layers and an essential reason for the accurate prediction of the flow over the rear window. The faster transition in the SBES model reduces the gray-area between the RANS and LES regions and the turbulent viscosity in the LES region, making it possible to resolve more and smaller turbulent structures than seen for the DDES model. The SBES model also ensures sufficient shielding of the RANS region, making it a more straightforward model to use than the DDES and IDDES models, as the user needs to be less aware of grid-induced effects. Lack of sufficient shielding is seen for the DDES model just upstream the rear window, where grid refinements cause the LES mode to be active within the near-wall region, where RANS is preferred. This results in underresolved turbulent stresses and overprediction of the separation over the rear window.

With the growing importance of high accuracy prediction of forces, the lack of consistent accuracy seen for the DDES and IDDES models show the need for hybrid RANS-LES models with sufficient shielding and faster generation of resolved turbulence in the gray-area, such as the SBES model. These abilities of the SBES model makes it well suitable for aerodynamic simulations of vehicles and not just for achieving accurate prediction of forces, but also for other subjects connected to aerodynamics, e.g., aeroacoustic noise, soiling, and aerodynamic stability.

CRediT authorship contribution statement

P. Ekman: Writing - original draft, Formal analysis. **D. Wieser:** Writing - original draft. **T. Virdung:** Validation. **M. Karlsson:** Validation.

Declaration of competing interest

The authors declare that they have no known competing financial interests or personal relationships that could have appeared to influence the work reported in this paper.

Acknowledgments

References

Ahmed, S.R., Ramm, G., Faltin, G., 1984. Some Salient Features of the Time-Averaged Ground Vehicle Wake. SAE Technical Paper. Technical report.

Aranake, A.C., Lakshminarayan, V.K., Duraisamy, K., 2015. Computational analysis of shrouded wind turbine configurations using a 3-dimensional rans solver. Renew. Energy 75, 818–832.

Ashton, N., Revell, A., 2015. Comparison of rans and des methods for the drivaer automotive body. SAE Technical Paper. Technical report.

Ashton, N., Prosser, R., Revell, A., 2011. A hybrid numerical scheme for a new formulation of delayed detached-eddy simulation (ddes) based on elliptic relaxation. In: Journal of Physics: Conference Series, vol. 318. IOP Publishing, 042043.

Ashton, N., West, A., Lardeau, S., Revell, A., 2016. Assessment of rans and des methods for realistic automotive models. Comput. Fluids 128, 1–15.

Ashton, N., Unterlechner, P., Blacha, T., 2018. Assessing the Sensitivity of Hybrid Rans-Les Simulations to Mesh Resolution, Numerical Schemes and Turbulence Modelling within an Industrial Cfd Process. SAE Technical Paper. Technical report.

Audi, A.G., 2019. How aerodynamics influence an electric car's range. https://www.audi.com/en/experience-audi/mobility-and-trends/e-mobility/e-tron-aerodynamic.html . (Accessed 14 October 2019).

Bello-Millan, F., Mäkelä, T., Parras, L., Del Pino, C., Ferrera, C., 2016. Experimental study on ahmed's body drag coefficient for different yaw angles. J. Wind Eng. Ind. Aerod. 157, 140–144.

Catalano, P., Tognaccini, R., 2011. Rans analysis of the low-Reynolds number flow around the sd7003 airfoil. Aero. Sci. Technol. 15 (8), 615–626.

Cheng, S.-Y., Chin, K.-Y., Mansor, S., Rahman, A.B.A., 2019. Experimental study of yaw angle effect on the aerodynamic characteristics of a road vehicle fitted with a rear spoiler. J. Wind Eng. Ind. Aerod. 184, 305–312.

Collin, C., Mack, S., Indinger, T., Mueller, J., 2016. A numerical and experimental evaluation of open jet wind tunnel interferences using the drivaer reference model. SAE Int. J. Passenger Cars Mech. Syst. 9, 657–679 (2016-01-1597).

D'Hooge, A., Palin, R., Rebbeck, L., Gargoloff, J., Duncan, B., 2014. Alternative simulation methods for assessing aerodynamic drag in realistic crosswind. SAE Int. J. Passenger Cars Mech. Syst. 7, 617–625, 01-0599.

Ekman, P., Larsson, T., Virdung, T., Karlsson, M., 2019. Accuracy and Speed for Scale-Resolving Simulations of the Drivaer Reference Model. SAE Technical Paper. Technical report.

European Commission, 2016a. Transport emissions. https://ec.europa.eu/clima/policies/transport_en. (Accessed 10 October 2019).

European Commission, 2016b. Transport emissions. https://ec.europa.eu/clima/policies/transport/vehicles/cars_en. (Accessed 10 October 2019).

Facts, W.L.T.P., 2017. What is WLTP and how does it work? https://wltpfacts.eu/what-is-wltp-how-will-it-work/. (Accessed 14 October 2019).

Fuchs, M., Mockett, C., Sesterhenn, J., Thiele, F., 2020. The grey-area improved σ-ddes approach: formulation review and application to complex test cases. In: Progress in Hybrid RANS-LES Modelling. Springer, pp. 119–130.

Gaylard, A., Howell, J., Garry, K., 2007. Observation of Flow Asymmetry over the Rear of Notchback Vehicles. SAE Technical Paper. Technical report.

Germano, M., Piomelli, U., Moin, P., Cabot, W.H., 1991. A dynamic subgrid-scale eddy viscosity model. Phys. Fluid. Fluid Dynam. 3 (7), 1760–1765.

Gritskevich, M.S., Garbaruk, A.V., Schütze, J., Menter, F.R., 2012. Development of ddes and iddes formulations for the k-ω shear stress transport model. Flow, Turbul. Combust. 88 (3), 431–449.

Gritskevich, M.S., Garbaruk, A.V., Menter, F.R., 2013. Fine-tuning of ddes and iddes formulations to the k-ω shear stress transport model. Progr. Flight Phys. 5, 23–42.

Guilmineau, E., 2014. Numerical simulations of flow around a realistic generic car model. SAE Int. J. Passenger Cars Mech. Syst. 7, 646–653, 2014-01-0607.

Heft, A.I., Indinger, T., Adams, N.A., 2012. Introduction of a New Realistic Generic Car Model for Aerodynamic Investigations. SAE Technical Paper. Technical report.

Hinterberger, C., Garcia-Villalba, M., Rodi, W., 2004. Large eddy simulation of flow around the ahmed body. In: The Aerodynamics of Heavy Vehicles: Trucks, Buses, and Trains. Springer, pp. 77–87.

Hucho, W., Sovran, G., 1993. Aerodynamics of road vehicles. Annu. Rev. Fluid Mech. 25 (1), 485–537.

Jasak, H., Weller, H., Gosman, A., 1999. High resolution nvd differencing scheme for arbitrarily unstructured meshes. Int. J. Numer. Methods Fluid. 31 (2), 431–449.

Kawamata, H., Kuroda, S., Tanaka, S., Oshima, M., 2016. Improvement of Practical Electric Consumption by Drag Reducing under Cross Wind. SAE Technical Paper. Technical report.

Krajnović, S., Davidson, L., 2004. Large-eddy Simulation of the Flow Around Simplified Car Model. SAE Technical Paper. Technical report.

Lanfrit, M., 2005. Best Practice Guidelines for Handling Automotive External Aerodynamics with FLUENT.

Lawson, N.J., Garry, K.P., Faucompret, N., 2007. An investigation of the flow characteristics in the bootdeck region of a scale model notchback saloon vehicle. Proc. Inst. Mech. Eng. - Part D J. Automob. Eng. 221 (6), 739–754.

Le Good, G.M., Garry, K.P., 2004. On the Use of Reference Models in Automotive Aerodynamics. SAE Technical Paper. Technical report.

Leonard, B., 1991. The ultimate conservative difference scheme applied to unsteady one-dimensional advection. Comput. Methods Appl. Mech. Eng. 88 (1), 17–74.

Menter, F.R., 1994. Two-equation eddy-viscosity models for engineering applications. AIAA J. 32 (8), 1598–1605.

Menter, F., 2016. Stress-blended eddy simulation (sbes)—a new paradigm in hybrid rans-les modeling. In: Symposium on Hybrid RANS-LES Methods. Springer, pp. 27–37.

Mockett, C., 2009. A Comprehensive Study of Detached Eddy Simulation. Univerlagtuberlin.

Nicoud, F., Toda, H.B., Cabrit, O., Bose, S., Lee, J., 2011. Using singular values to build a subgrid-scale model for large eddy simulations. Phys. Fluids 23 (8), 85106.

Palin, R., Johnston, V., Johnson, S., D'Hooge, A., Duncan, B., Gargoloff, J.I., 2012. The Aerodynamic Development of the Tesla Model S-Part 1: Overview. SAE Technical Paper. Technical report.

Rodi, W., 1997. Comparison of les and rans calculations of the flow around bluff bodies. J. Wind Eng. Ind. Aerod. 69, 55–75.

SAE Standard J2966, 2013. Guidelines for aerodynamic Assessment of medium and heavy commercial ground vehicles using computational Fluid dynamics. *SAE international surface vehicle recommended practice*. SAE Int. https://saemobilus.sae.org/content/j2966_201309.

Sagaut, P., 2013. Multiscale and Multiresolution Approaches in Turbulence: LES, DES and Hybrid RANS/LES Methods: Applications and Guidelines. World Scientific.

Serre, E., Minguez, M., Pasquetti, R., Guilmineau, E., Deng, G.B., Kornhaas, M., Schäfer, M., Fröhlich, J., Hinterberger, C., Rodi, W., 2013. On simulating the turbulent flow around the ahmed body: a French–German collaborative evaluation of les and des. Comput. Fluids 78, 10–23.

Shur, M.L., Spalart, P.R., Strelets, M.K., Travin, A.K., 2008. A hybrid rans-les approach with delayed-des and wall-modelled les capabilities. Int. J. Heat Fluid Flow 29 (6), 1638–1649.

Sims-Williams, D., Marwood, D., Sprot, A., 2011. Links between notchback geometry, aerodynamic drag, flow asymmetry and unsteady wake structure. SAE Int. J. Passenger Cars Mech. Syst. 4 (1), 156–165.

Spalart, P.R., 1997. Comments on the feasibility of les for wings, and on a hybrid rans/les approach. In: Proceedings of First AFOSR International Conference on DNS/LES. Greyden Press.

Spalart, P., Allmaras, S., 1992. A one-equation turbulence model for aerodynamic flows. In: 30th Aerospace Sciences Meeting and Exhibit, p. 439.

Spalart, P.R., Deck, S., Shur, M.L., Squires, K.D., Strelets, M.K., Travin, A., 2006. A new version of detached-eddy simulation, resistant to ambiguous grid densities. Theor. Comput. Fluid Dynam. 20 (3), 181.

Sterken, L., Sebben, S., Löfdahl, L., 2016. Numerical implementation of detached-eddy simulation on a passenger vehicle and some experimental correlation. J. Fluid Eng. 138 (9), 91105.

Strangfeld, C., Wieser, D., Schmidt, H.-J., Woszidlo, R., Nayeri, C., Paschereit, C., 2013. Experimental Study of Baseline Flow Characteristics for the Realistic Car Model Drivaer. SAE Technical Paper. Technical report.

Tunay, T., Drugge, L., O'Reilly, C.J., 2020. On coupling methods used to simulate the dynamic characteristics of heavy ground vehicles subjected to crosswind. J. Wind Eng. Ind. Aerod. 201, 104194.

Wang, S., Avadiar, T., Thompson, M.C., Burton, D., 2019. Effect of moving ground on the aerodynamics of a generic automotive model: the drivaer-estate. J. Wind Eng. Ind. Aerod. 195, 104000.

Wieser, D., Schmidt, H.-J., Müller, S., Strangfeld, C., Nayeri, C., Paschereit, C., 2014. Experimental comparison of the aerodynamic behavior of fastback and notchback drivaer models. SAE Int. J. Passenger Cars Mech. Syst. 7, 682–691, 2014-01-0613.

Wieser, D., Lang, H., Nayeri, C., Paschereit, C., 2015a. Manipulation of the aerodynamic behavior of the drivaer model with fluidic oscillators. SAE Int. J. Passenger Cars Mech. Syst. 8, 687–702, 2015-01-1540.

Wieser, D., Nayeri, C., Paschereit, C.O., 2015b. Experiments with vortex generators applied to a notchback car model. AIAA Aerospace Sciences Meeting, p. 1236.

Windsor, S., 2014. Real world drag coefficient-is it wind averaged drag?. In: The International Vehicle Aerodynamics Conference. Woodhead Publishing, p. 3.

Zhang, C., Tanneberger, M., Kuthada, T., Wittmeier, F., Wiedemann, J., Nies, J., 2019. Introduction of the Aerosuv-A New Generic Suv Model for Aerodynamic Research. SAE Technical Paper. Technical report.

Glossary

A: projected frontal area of the car body [m^2]
B_i: Bifurcation line
C_D: Drag force coefficient
C_f: Skin friction coefficient
C_L: Lift force coefficient
C_P: Static pressure coefficient
$C_{P.RMS}$: Static fluctuating pressure coefficient
F_D: Drag force [N]
F_L: Lift force [N]
F_i: Focus points
H: height of the car body [m]
L: Length of the car body [m]
k_{res}: Resolved turbulent kinetic energy
p: pressure
p_∞: Free-stream pressure [Pa]
S_i: Saddle point
U_∞: Free-stream air velocity

U_i: Unstable node
y^+: Dimensionless wall distance
Δt: time-step size [s]
ρ_∞: Free-stream air density [kg/m^{-3}]
φ: Percentage solid blockage in test-section
τ: Wall shear stress

Subscripts
CFD: Computational Fluid Dynamics
CFL: Courant-Friedrichs-Lewy
CO_2: Carbon Dioxide
EV: Electric Vehicle
DES: Detached Eddy Simulation
DDES: Delayed Detached Eddy Simulation
ICE: Internal Combustion Engine
IDDES: Improved Delayed Detached Eddy Simulation
LES: Large Eddy Simulation
NEDC: New European Driving Cycle
PIV: Particle Image Velocimetry
RANS: Reynolds Average Navier-Stokes
SBES: Stress Blended Eddy Simulation
SIMPLEC: Semi-Implicit Method for Pressure linked Equations-Consistent
SRS: Scale-Resolving Simulation
SST: Shear Stress Transport
TKE: Turbulent Kinetic Energy
WLTP: Worldwide Harmonized Light Vehicles Test Procedure
WMLES: Wall-Modeled Large Eddy Simulation